MECHANICAL BEHAVIOR OF FRICTION STIR EXTRUDED TUBES

by

Abdulla Taoufik Alhourani

A Thesis presented to the Faculty of the
American University of Sharjah
College of Engineering
In Partial Fulfillment
of the Requirements
for the Degree of

Master of Science in
Mechanical Engineering

Sharjah, United Arab Emirates

December 2020

Declaration of Authorship

I declare that this thesis is my own work and, to the best of my knowledge and belief, it does not contain material published or written by a third party, except where permission has been obtained and/or appropriately cited through full and accurate referencing.

Signed……...…Abdulla Taoufik Alhourani….…….

Date…….…….……13-12-2020……...……...….……..…

Approval Signatures

We, the undersigned, approve the Master's Thesis of Abdulla Taoufik Alhourani

Thesis Title: Mechanical Behavior of Friction Stir Extruded Tubes.

Date of Defense: 13-12-2020

Name, Title and Affiliation	**Signature**
Dr. Mohammad Ahmad Hasan Nazzal Associate Professor, Department of Mechanical Engineering Thesis Advisor	
Dr. Basil Mohammad Darras Associate Professor, Department of Mechanical Engineering Thesis Co-Advisor	
Dr. Maen Abdelqader Alkhader Associate Professor, Department of Mechanical Engineering Thesis Committee Member	
Dr. Mahmoud Ismail Awad Associate Professor, Department of Industrial Engineering Thesis Committee Member	
Dr. Mamoun Abdel-Hafez Head Department of Mechanical Engineering	
Dr. Lofti Romdhane Associate Dean for Graduate Studies and Research College of Engineering	
Dr. Sirin Tekinay Dean College of Engineering	
Dr. Mohamed El-Tarhuni Vice Provost for Graduate Studies Office of Graduate Studies	

Acknowledgement

First of all, this research would not have been completed this far without the blessings of Allah for granting me this opportunity to do my masters at AUS and serving as a graduate teaching assistant. I want to express my sincere gratitude to my advisors Dr. Mohammad Nazzal and Dr. Basil Darras in the mechanical engineering department for their supervision, guidance, support and motivation throughout my research stages.

I would like to thank the faculty of mechanical engineering department who I took graduate courses with for their profound teaching efforts and skills and greatly appreciate their advices. In addition, I would like to extend my thanks to the thesis defense committee examiners, Dr. Maen Alkhader and Dr. Mahmoud Awad, for their valuable inputs.

I am grateful for the mechanical department for providing me with equipped laboratory to run my experiments with the assistance of the manufacturing lab operators, Mr. Dennis Pusing and Mr. Ronald Almirez, and material science lab Eng. Mohammad Mustafa.

Lastly, I am deeply thankful and in gratitude to my family for their continuous encouragement and support during my research process.

Dedication

To my family for always bringing out the best in me…

Abstract

Friction Stir Back Extrusion (FSBE) is a new grade of severe plastic deformation processes capable of producing metallic tubular geometries that exhibit ultrafine grain structure and superior mechanical properties. FSBE of tubular sections provide opportunities for producing lightweight rigid structures for the automotive, aerospace and construction industries. This research investigates the impact of rotational speed and feed rate on the mechanical properties, power consumption and cycle time for FSBE of Magnesium AZ31-B tubes under air cooling medium to determine the optimal settings. The investigation is conducted utilizing Response Surface Methodology (RSM) and desirability multi-response optimization technique. RSM results suggest that the ultimate tensile strength and toughness are impacted by both rotational speed and feed rate and are more sensitive to spindle rotational speed. Yet, both parameters did not show a significant statistical impact on percent elongation. The optimal settings to maximize mechanical properties and minimize production indicators are 2000 rpm and 116 mm/min. Furthermore, the effect of submerging conditions (in water at 25 °C and 2 °C) on the grain size and mechanical properties was investigated and compared to FSBE in air. It is shown that the impact of submerging is statistically insignificant in terms of the mechanical properties of the produced tubes. On the other hand, finer grains were observed at the inner wall of the tube for FSBE in air and underwater FSBE at 25 °C when compared to underwater FSBE at 2 °C.

Keywords: ***Friction Stir Back Extrusion; Magnesium Alloy; RSM Optimization; Submerged FSBE; Mechanical Properties; Microstructure.***

Table of Contents

List of Figures

List of Tables

Chapter 1. Introduction

In this chapter, a short explanation of the different types and variations of SPD starting from the simple extrusion process and ending with FSBE in terms of their working mechanism and application is introduced. Consequently, the research contribution and thesis objectives are presented to outline the significance of the conducted research.

1.1. Overview

Manufacturing in its numerous processes is a vital aspect in today's industries. Metal forming processes are mainly categorized into sheet metalworking and bulk deformation as the latter includes extrusion, forging, rolling and many more that are one of the oldest and current processes the technological world cannot proceed without for any simple product. Processes such as extrusion are very complicated as they induce large plastic strain deformation. Extrusion is a bulk forming process where the specimen is pushed into the die opening to form the shape of its cross section [1]. Furthermore, different types of this process include cold and hot working besides friction extrusion. Apparently, the difference between the hot and cold working is the temperature at which the process operates at as the former is performed at a temperature higher than the recrystallization temperature of the workpiece and vice versa for cold working [1].

Friction extrusion (Figure 1) is a thermo-mechanical process that can be used to form a wide range of shapes by severe plastic deformation (SPD) such as rods, tubes and other non-circular geometries directly from the variety of precursor charges including a solid billet and metal powder or even flakes [1]. The process has a desirable impact on the microstructures of the resulting end products [2,3]. Moreover, friction extrusion involves the spinning of the metal billets based on the die's location. As the die rotates, it produces heat from the surface-to-surface friction around the entry of the die whereas the heat softens the metal which allows it to pass easily through the die. It was originally intended as a method for production of homogenized microstructures in lightweight Magnesium and Aluminum Metal Matrix Composites (MMC) [1].

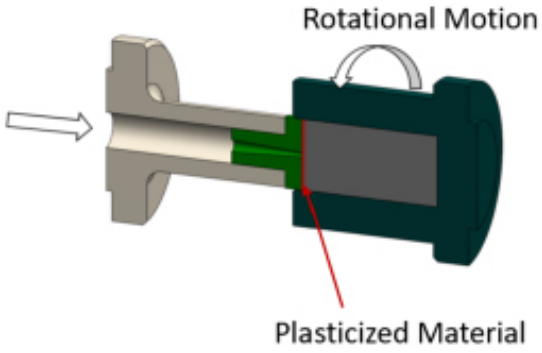

Figure 1: Horizontal Friction Extrusion Process [2]

In addition, Friction Stir Welding (FSW) is a solid-state welding process developed by the Welding institute [1]. It uses non-consumable cylindrical rotating tool to create a weld joint by stirring the contact line between the two metal plates, therefore no melting is needed to create the joint. Although friction extrusion and FSW fall under the process of SPD, however each one has its own mechanism and results in a different geometry. Such technique can be applied to many metals such as Copper, Titanium, Magnesium and many more resulting in high quality welds and more energy efficient process than traditional joining techniques [2]. Friction Stir Processing (FSP) is a successor of FSW (Figure 2) which is indeed similar to the latter method, however in FSP the rotary non-consumable tool crosses through one workpiece without reaching the material's melting point. It is implemented to manipulate and refine the material's properties. For example, to achieve excellent mechanical properties, alter the microstructure and increase resistance to corrosion.

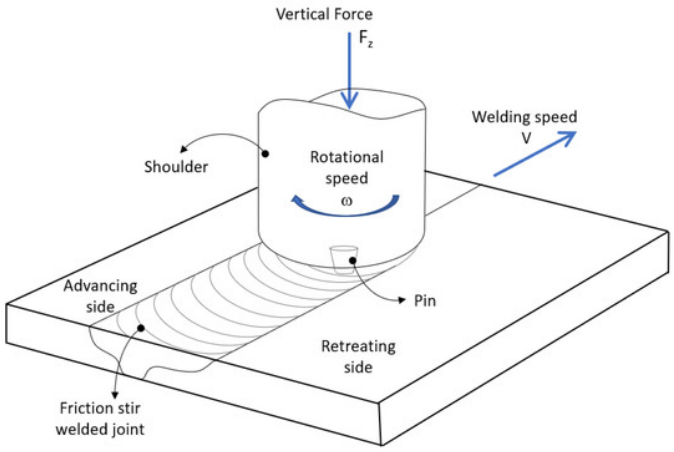

Figure 2: Schematic diagram of FSW process [4]

Due to the adverse effects of high frictional heat generated during FSW on the mechanical properties and grain structure of the welded plate(s), the cooling rate needs to be controlled and improved using multiple cooling methods [5,6]. Such a process is referred to as Submerged FSW or SFSW which is FSW operated under a cooling medium such as liquid water (Figure 3) with its various temperatures (cold water, room temperature and hot water) in addition to liquid nitrogen. This method can be applied to similar and dissimilar metal alloys such as Magnesium and Aluminum alloys.

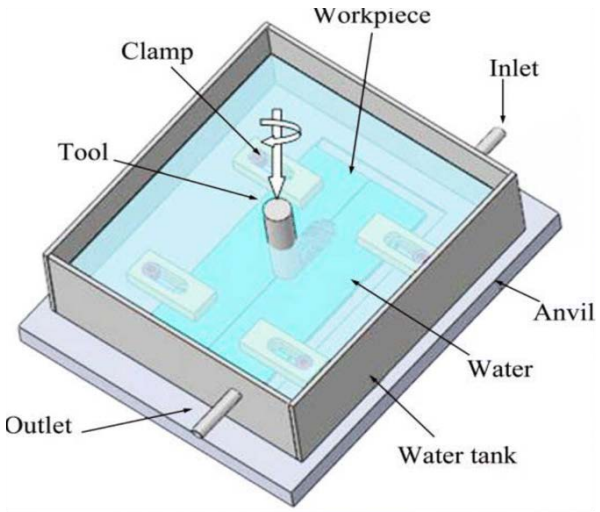

Figure 3: SFSW fixture [7]

Recently, a new SPD route has been introduced which is FSBE that produces tubular shapes with equiaxed grain structure and desirable mechanical properties, for example higher ductility. FSBE is quite new as it is developed by Fadi Abu-Farha back in 2012, which is based on the friction stirring phenomenon that is known as Spiral Friction Stir Processing (SFSP) [8]. SFSP is mainly applied to bulk material with the stirring tool rotating and moving along the axial direction so it combines both motions which will induce a spiral material flow [8,9]. This process can be applied to MMCs and metal alloys such as Aluminum and Magnesium alloys as they have a promising future in the vast lightweight applications in many industries. Such type of extrusion is an effective and efficient process that is gaining popularity among manufacturers.

It is said to be a challenge for manufactures to choose the most effective process parameters associated with the novel FSBE as its history is still not rich enough which deems further exploration. Although recent research evaluated the FSBE process with

the material performance of Mg AZ31-B such as Milner and Abu-Farha [10], however their analysis is based on a fixed rotational speed and feed rate. Therefore, to achieve structurally sound tubes and desirable mechanical properties with low energy consumption, an optimization technique is to be implemented. There are various methods to model and optimize an FSBE process which defines the desired output variables through mathematical models that set a relation between the input parameters and output variables [11]. One of those can be named as RSM. But many researchers use the standard experimental procedure which is changing one process parameter while keeping other parameters fixed and observing its effect [12]. This conventional method is considered to be time consuming and material wasting, thus the use of a proper optimization technique is desired. RSM is a mathematical and statistical approach used to optimize several process parameters that affect one or more response variables with fewer experimentations through a Design of Experiment (DOE) [13, 14]. Among the various classes of RSM, Central Composite Design (CCD) is the most popular with its response surface designs (Figure 4). The variations are Central Composite Circumscribed (CCC), Central Composite Inscribed (CCI) and Face Centered Cube (FCC) [15]. The first two types are valid for a minimum of 3 factors with 5 levels while FCC is applicable for a minimum of 2 design parameters with 3 levels. CCC is said to give highly accurate predictions as the design is considered to be rotatable which means that the design points are uniformly distributed over the design space having the same alpha (α), distance between the axial (star) points and the center point, and this induces consistent and minimal prediction variance of the model's coefficients [15]. Rotatable surface designs have an α value of $\pm\sqrt{k}$ and k is the number of factors; and this value is more than 1. In other words, α determines the low and high limits of the design levels in a coded format. On the other hand, FCC is reflected as a near rotatable design as it does not require data points outside the factorial space which indicates its simplicity having an α of ±1 [15]. Face centered CCD provides relative high accuracy compared to CCC for a smaller number of experimentations (star points are at the center of each face) which makes it a simpler design to implement. Moreover, data analysis and the development of the mathematical relations can be implemented through Analysis of Variance (ANOVA). To find the optimal process parameters, in other words to maximize/minimize certain desired outputs, desirability multi response

optimization technique can be used. Such a DOE method can generate experiment designs and analysis using statistical software programs such as Minitab.

1.2. Research Motivation

The demand of lightweight applications with limited environmental impact in many industrial sectors such as aerospace, biomedical and automotive has led to increased research in the field of light-weighting [16-18]. Magnesium is said to be the lightest construction metal on earth. Therefore, the use of Mg with its alloys are of benefit in vast applications including bone scaffolds, high temperature energy absorptions, catalysts, light weight sandwich, tubular structures and many more due to their high strength to weight ratios with lower densities. However, Mg alloys exhibit low formability as a consequence of their hexagonal closed packed lattice and pronounced plastic anisotropy [19,20]. As a result, hot forming such as superplastic forming has been used to form Mg alloy sheets and other difficult to form alloys [21-30]. Using FSBE process in which heating of the processed alloy occurs due to plastic deformation and friction, fine grain size structure and homogenization is achieved in the stirring zone, the tube's inner diameter, which enhances the material's properties. It also exhibits less energy consumption compared to other tube extrusion processes [31].

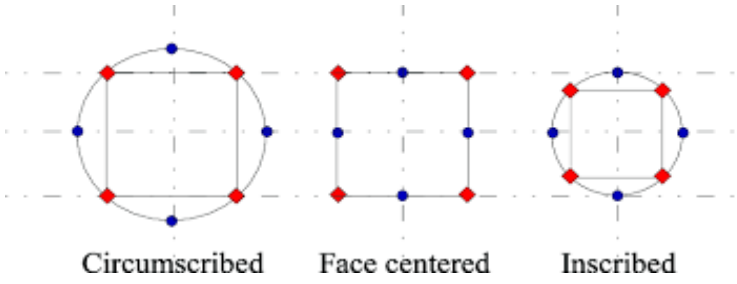

Figure 4: Types of CCD [32]

Although limited research had been conducted on FSBE tubes since its invention, the conducted studies mainly investigated the microstructural and mechanical behavior at one fixed parameter setting while little research, if any, was conducted to optimize FSBE process parameters. Accordingly, it is necessary to have a detailed understanding of FSBE AZ31-B tubes' behavior through RSM method and desirability multi-response optimization technique for the mechanical properties and productivity indicators. In addition, submerged FSBE at two cooling conditions are

analyzed and compared to natural cooling in terms of the mechanical behavior, microstructural analysis and thermal history.

1.3. Thesis Objectives

The objectives of this research work can be summarized as follows:

- Optimize and predict the mechanical properties namely, UTS, toughness and percent elongation, in addition to the power consumption and cycle time as production indicators by using the RSM statistical technique and desirability multi-purpose optimization method.
- Explore the behavior of the formed tubes submerged underwater by two different temperatures, room temperature (25 °C) and cold temperature (2 °C), through analysing its effect in terms of the mechanical properties, power consumption, thermal history and microstructure.

1.4. Thesis Organization

The rest of the thesis is organized as follows: Chapter 2 provides literature review about the recently used friction stir techniques ending with and mechanical studies of FSBE. Furthermore, Chapter 3 addresses the methodological approach used for the experimental measurements under different cooling mediums followed by Chapter 4 which provides details about the experimental setup including the milling machine fixture for separate cooling methods besides tensile. Chapter 5 provides details about the optimization and experimental results with their discussion. Finally, Chapter 6 summarizes the key findings and states the future work.

Chapter 2. Background and Literature Review

This chapter states the previous research done on FSW which is the closest to the idea of FSBE. The optimization of FSW in its various techniques are also mentioned. Additionally, the up to date conducted research on FSBE in terms of process evaluation and material performance of different alloys is presented besides the mechanical properties, microstructural analysis and hardness distribution of the extruded tubes.

2.1. Friction Stir Welding

The first used friction stir technique was FSW. It is considered as a solid-state welding process which uses heat induced by friction from the contact between the rotating probe and the workpieces. The rotating tool consists of two parts, pin and shoulder, in which the pin is responsible for mixing both materials together to form a weld joint whereas the shoulder acts for generating frictional heat as it will cause thermal softening without material melting to plastically deform both workpieces along the weld line [33]. The softening will increase the plastic deformation leading to SPD hence dynamic recrystallization and eventually grain refinement. The stirring tool plunges and rotates at a specific depth and speed, respectively with a specified traverse speed. Such technique has proved itself with respect to many hard to weld metals, in particular the 5000 Aluminium alloys and the hard to weld 2000 and 7000 Aluminium alloys. This welding method results in seamless welds without defects besides improved mechanical properties compared to other traditional joining techniques such as friction welding [33]. Therefore, FSW has attracted global attention for its expansion to various monolithic metals besides Aluminium and deserved its place in multiple industries such as aerospace and automotive.

Literature is rich of research related to FSW. For example, several researchers suggested that SPD associated with FSW process creates superior fatigue properties, improved formability and equiaxed grain structure in the weld zone [34-39]. Cavaliere et al. [36] indicated that average grain size of FSW AA 6056 alloy is from 4 μm to 5 μm whereas Hatamleh et al. [37] reported an average grain size of FSW AA 7075 alloy between 5 μm to 12 μm. Moreover, FSW has been used to refine the weld zone's microstructure using a rotating stirring tool that crosses a single plate [40]. Several SPD

processes were explored by researchers to manufacture materials with equiaxed grain structure. Such processes include cyclic extrusion compression, equal channel angular pressing, tube channel pressing and high-pressure tube twisting; however, only the earlier two are said to produce tubular shapes with ultrafine grain size [41-43]. Such method has been more involved into material characterization than welding as it can improve the superplastic behavior of the extruded tubes and creates microstructure homogeneity among the stirring zone.

2.2. Optimization in FSW

Other researchers focused on FSW process parameters' effect on mechanical properties of welded material. Verma and Misra [44] studied the effects of the rotational speed, welding speed and tilt angle on the temperature distribution and force during FSW. Two phenomenological models were utilized to evaluate the effect of process parameters on the force and temperature. Iqbal et al. [45] investigated the influence of FSW process parameters on the physical properties of Aluminum pipes. The temperature, axial force, torque and power have been investigated to select optimum combination of parameters and achieve superior welds. Jain et al. [46] examined the effect of pin shapes on temperature distribution, material flow and forces during FSW using simulation. Triflat, cylindrical and square pin shapes were used in the simulations. The Triflat pin produced higher temperatures and strain rates which resulted in uniformly distributed material deposition. Rambabu et al. [47] investigated the impact of FSW process parameters on AA 2219 Aluminum alloy corrosion rate. They concluded that tool profile, rotational speed, welding speed and axial force have significant impact on corrosion rate. Zhang et al. [48] analyzed the effect of transverse speed, plunge depth and rotational speed on corrosion rate, yield strength, Ultimate Tensile Strength (UTS) and elongation for AA 2024-T351 and AA 7075-T651 dissimilar alloys. They also developed a mathematical model and verified it using Analysis of Variance (ANOVA) to determine the optimum set of process parameters to maximize tensile properties and corrosion rate. On the other hand, Kabiri and Ehsan [49] used Taguchi Orthogonal Arrays (OA) to investigate the impact of rotational speed, traverse speed and shoulder surface diameter on UTS for pure Copper. They suggested that all process parameters had similar contributing effect on UTS. Similarly, Kumar et al. [50] used Taguchi OA to optimize FSW process parameters for dissimilar Aluminum alloys. Others including Abbasi et al. [51] utilized the previous optimization

technique to optimize the traverse speed, rotational speed and tool profile of FSW AA 5052 alloy for maximizing the tensile strength. They concluded that the squared profile is the dominant contributing factor among others besides having the probe shape as the most significant parameter. Additionally, de Castro et al. [52] utilized Taguchi OA optimization approach to study the effect of the welding time, rotational speed and tool plunge depth of the weld's strength for the Fiction Stir Spot Welding (FSSW) of AA 2198-T8 Aluminum alloy. They concluded that tool's plunge depth and spindle speed have a significant effect on the induced strength. Colmenero et al. [53] optimized the FSSW for AA 1050 and pure copper using RSM method which primarily depends on dwell time and rotational speed process parameters. They examined vibration signals' energy and the welded joint strength. Finally, Babu et al. [54] used Artificial Neutral Networks with Genetic algorithm to optimize FSW process parameters for AA 2219 Aluminum alloy.

2.3. Submerged FSW

Although FSW exhibits many advantages with respect to fusion welding in its types where the metal specimens are being joined/fused by heating up the contact line until its melting temperature [55]. Such benefits include conducting the process under the metal's melting point with crack and void free samples acquiring improved mechanical properties. That being said, FSW has a downside in terms of its thermal history in which it was noted by many researchers [56,57] that thermal softening was observed in heat treated Aluminum alloys where the weld's strength degraded due to generated high heat. Therefore, cooling methods have been introduced in the SFSW process. A study by Fu et al. [58] investigated the cooling effect on the tensile strength and microhardness values under cold (8 °C) and hot (90 °C) water for AA 7050 alloy and compared the results with the air-cooled specimens. It was clear that the peak temperature dropped from 380 °C to 300 °C and further to 220 °C in the case of cold water. Also, the hardness values showed an increase from 105 HV to 114 HV and to 115 HV with respect to cold and hot water, respectively. The UTS of the SFSW under hot water achieved the highest value while the air induced the lowest. Darras and Kishta [59] studied the microstructure and mechanical properties of AZ31B-O sheets under hot (60-70 °C), cold water (room temperature) and air environments where the micrographs showed smaller grains under the effect of various cooling means. The grain sizes were 13.3 μm, 15.9 μm and 18.9 μm for the cold, hot and air-cooling

mediums, respectively. To add, the microstructure clearly shows the homogeneity across all samples compared to the as received material which exhibits bigger grains. The mechanical properties indicated that the lowest ductility took place with the cold water, however much more than the as received Mg alloy whereas the hot water captures the longest ductility. On the other hand, the power consumption across all the three cooling modes did not show any significance.

Others such as Mofid et al. [60] examined welding dissimilar metal plates of AA 5083-H83 and Mg AZ31 alloys under liquid nitrogen of -40 °C besides liquid water and air. They induced that SFSW through water and liquid nitrogen lowered the peak temperature to 389 °C and 382 °C from 435 °C and hence the intermetallic compounds are hindered and stopped from expanding resulting in a uniform interface along the stir zone. Moreover, the high Vickers hardness values were recorded in the air-cooled plate which is linked to the microstructure being adversely affected due to coarse grains by the high peak temperature during the process. On the contrary, using both cooling mediums showed lower microhardness values. The strength of weld joints showed improved value for liquid nitrogen and under water with UTS of 134 MPa and 167 MPa, respectively. Additionally, Zhang and Liu [61] investigated the defects due to the weld of AA 2219-T6 underwater with various process parameters. It was realized that defects exist in high and low rotational speeds from 600 rpm to 1400 rpm. In low spindle speeds, the heat generated is the main reason behind the defect formation whereas in high rotational speeds it depends on the welding speeds [61]. In case it is high, the thermo-mechanical affected zone is pulled towards the weld hole which further makes the shoulder's sheared zone to flow in the direction of the pin stirred zone. According to Chandran and Santhanam [62], who explored the mechanical properties, macrostructural analysis and microhardness of FSW underwater with different water heads, 0 mm (no water head), 10 mm, 20 mm and 30 mm for AA 6061-T6 alloy. The results showed an increase in power consumption in water cooled welds compared to air cooled FSW. SFSW proved its effectiveness in being conducted in higher rotational speeds than FSW without the occurrence of defects. In addition, the characterization of the mechanical properties indicated an increase in the tensile strength across all water heads, however the highest was achieved through a water head of 20 mm [62]. Due to the achieved fine grain structure, HV values were higher in the thermo-mechanical and nugget zones when put aside with natural cooling.

The above authors implemented the RSM optimization method to attain the highest UTS of the SFSW of similar AA 6061-T6 plates [63]. They varied three process parameters namely, the welding speed, rotational speed and water head. The optimal response was recorded to be 211 MPa given 30 mm/min, 1200 rpm and 10 mm, respectively. The submerged peak temperature is 95 °C near the weld compared to 228 °C for the naturally cooled FSW. A refined average grain size of 2.5 μm was also reached while the air cooled FSW had a size of 7 μm. Finally, Peng et al. [64] did not explicitly do the experiments under liquid water or liquid nitrogen, instead they used compressed air as a cooling technique in comparison with natural cooling on dissimilar 5A 06-H112 and 6061-T651 Aluminum alloys. Microstructural, tensile and hardness properties were investigated as a two-level tensile strength decease was observed for both cooling methods when compared with the base metal for various welding and rotational speeds in which a 10 % increase was noted for forced air. That being said, forced air cooled method showed a higher cooling rate which affects the generated heat due to temperature that prevents grain growth leading to improved UTS [64]. Although AA 6061 exhibits low hardness values due to precipitate dissolution with normal cooling, increased hardness values were evident in the heat affected zone of the former metal alloy due to forced air cooling which further agrees with the induced grain refinement.

2.4. Friction Stir Back Extrusion

A new SPD friction stir process that is considered a derivative of FSW known as FSBE is developed. FSBE is used to produce seamless tubular shapes with ultrafine grain structure and improved mechanical properties. The FSBE process is depicted in Figure 5 where a non-consumable stirring tool rotates and plunges through a cylindrical metal billet inducing spiral material flow. The self-induced heat generated due to friction between the stirring tool and the specimen softens the material aiding in the outward material flow and forming a tubular shaped structure [65]. Consequently, the load needed to force the stirring tool into the billet is significantly less than other SPD processes such as cold extrusion. Such tubular shapes can be used in various industries including aerospace and automotive [66]. For instance, the processed seamless tubes can be used as roof rails and as structural members in compressive load bearing applications such as automotive frames. According to the sustainability assessment framework proposed by Saad et al. [67], FSW and FSBE are said to be sustainable

manufacturing processes in terms of their environmental, social and economic dimensions [68, 69].

Several researchers used FSBE process to produce tubes with an equiaxed grain structure using different materials. For example, Abu-Farha [8] used AA 6063-T52 in FSBE to produce void free tubes with highly desirable microstructure. Similarly, Milner and Abu-Farha [32] evaluated the microstructure and mechanical properties for different AZ31-B tube aspect ratios (tube length / outer diameter) and extrusion ratios (outer diameter / inner diameter). They concluded that FSBE tubes requires less energy to operate as it induces heat from within the process compared to other back extrusions methods. In addition, they confirmed that the AZ31-B FSBE tubes has an ultra-fine grain of around 5 μm compared to the base material of around 114 μm within the mixing zone [32]. Evaluation of mechanical properties indicated an increase in UTS, yield strength and ductility. The same authors made a connection between the induced grain size and micro hardness values at different locations within the dynamically recrystallized zone for AZ31-B tubes. They found that measurements at the bottom center of the tube showed high micro hardness values which corresponds to finer grains relative to low micro hardness values at different sections within the tube's wall. Mathew et al. [70] studied the compressive behavior of AA 6061 processed tubes and showed a ring (concertina) failure type which is most favorable for Aluminum tubes [71]. This indicates that processed tubes will be able to absorb sufficient amount of energy before failure.

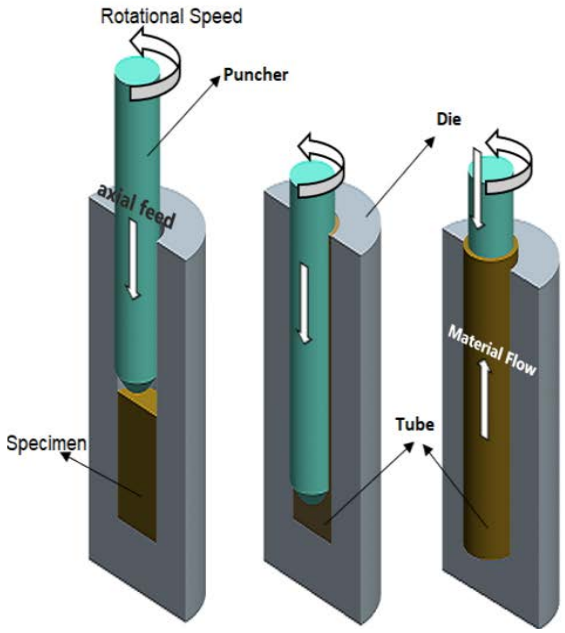

Figure 5: Schematic diagram of FSBE with required parts [72]

Emblom et al. [73] explored the miniaturization of FSBE for the applications of meso and micro scale tubing such as microscale heat exchanger. They focused on macro tooling for processed tubes of higher length to diameter ratios and successfully built tubes with 50 mm and 12.5 mm in length and outer diameter, respectively. Various stirring tool designs were also tested for different rotational speeds; however, the successful tooling design included a guide plate with brass bushing for alignment and dowels that are fixed to the split dies [73]. Such design reduced the tool's end deflection as it pushes through the workpiece in addition to the increase in the buckling force.

2.4.1. Metallography and fractography in FSBE. Since the invention of FSBE, many researchers examined and analyzed the microstructure of the extruded tubes. Microstructural characterization helps in determining key information about how the tube was processed due to the stirring tool's spiral motion at different locations across the tube's thickness and along its wall. Abu-Farha [8] was the first one to conduct grain structural analysis for FSBE tubes, it was examined on AA 6063-T52 tubes at different processed locations at the stirring zone of the tubes, such as the base's center. The center of the base resulted in significant fine grains that are in average lower than 15 μm and increasing in size as the distance is further from the base reaching up 80 μm. Besides that, analysis on the base's corner (outer tip of the tool) showed very similar grain size evolution as the center of the base. It is noted that an intermediate zone exists between the stirring zone and the undeformed/unprocessed material which contains several elongated grains that reach out to 200 μm in the tool's rotational speed direction [8]. Furthermore, a higher location at the inner wall is investigated to have higher equiaxed grains of around 35 μm while increasing to 55 μm outwards from the inner wall.

As mentioned earlier, Milner and Abu-Farha [32] characterized the metallography of the AZ31-B alloy tubes for the as received rod and the extruded tubes. The as received rod had a variation of the grain size ranging from 55 μm to 157 μm with some grains having a size of 200 μm from the outer edge to the following zone while the center of the rod reveals a slight lower grain size than the second zone but a clear heterogeneous structure is present [32]. A very similar trend in the grain size evolution and micrographs of AA 6063-T52 is apparent in the Mg AZ31-B alloy tubes at the base's center and corners for average sizes of 5 μm and 7 μm. Along the wall,

analysis was conducted at 3 different heights (5 mm, 20 mm and 40 mm) above the base which showed a gradual increase in the grain size of 10 μm, 13 μm and 11 μm, respectively due to grain coarsening [32]. The average grain size of the extruded tube indicates that there is a 90% drop in size compared to the as received so an equiaxed grain structure with a homogenous structure exist. The authors subdivided the zones of the tube's thickness into 4 zones starting from the inner zone which is stirring zone and ending with the outer layer. The middle zones are presented as an intermediate zone having a dynamically recrystallized structure and a heterogeneous zone with elongated grains.

Mathew et al. [70] investigated AA 6061-T6 FSBE seamless tubes and showed that the process resulted in a continuous defect free tubes with an average grain size of 39 μm for multiple locations along the tube's wall and 3.5 μm and 20 μm for the stir zone (base) and parent alloy, respectively. On the other hand, Jamali et al. [74] conducted FSBE tests for AA 6063 Aluminum alloy wires for three differently rotated specimens of 300 rpm, 475 rpm and 600 rpm where the microstructural investigation showed a decrease in the grain size from the as received alloy of 179 μm to 40.1 μm, 15.5 μm and 21.9 μm, respectively. This also revealed that the induced temperature in the 300-rpm test is low for a longer duration which presented grain growth while high heat generation at 600 rpm similarly results in grain coarsening [74]. However, the 475-rpm extruded wire had sufficient frictional heat for the completion of recovery and recrystallization that ended up with significant grain refinement which in fact exhibits the lowest size.

Although Milner and Abu-Farha [75] and Khorrami and Movahedi [66] conducted uniaxial tensile tests for the formed tubes, they did not examine the fractured surface. Such analysis helps in determining the fracture type and its initiation point, the existence of voids or not and many more characteristics.

2.4.2. Micro-hardness analysis. Vickers hardness tests were conducted for the extruded tubes at different locations, including the wall, base's center and corners, from the stirring zone to the unheated zone (parent alloy). Such measurements and analysis were studied by Milner and Abu-Farha [32] who reported the variation in the HV (Hardness Vickers) values at the center of the tube vertically below the stirring tool besides the values across the wall thickness at 4 different heights (0 mm, 10 mm, 20

mm and 30 mm) from the tool's base. They concluded that the stirring zone exhibit higher Vickers values which are inversely proportional with the grain size hence ultra-fine grains exist. Others such as Jamali et al. [74] investigated the Vickers micro-hardness analysis of FSBE AA 6063 wires with the base material and resulted in values of 53.7 HV, 61.4 HV and 58.7 HV for 300 rpm, 475 rpm and 600 rpm, respectively while a value 54.8 HV is for the base metal. Since the 300-rpm wire has the highest HV then it reveals an equiaxed grain structure. Khorrami and Movahedi [66] reported HV values for two locations, across the wall's thickness and across the middle point in the tapered area, with 4 different layers. The authors classified the zones from the inner to outer zone as dynamic recrystallized region, static recrystallized region, partially static recrystallized region and finally the heated extruded base metal. The micro-hardness values were found to be similar across all zones even in the parent Aluminum alloy having an average HV value of 73. Comparatively, the heated base material showed a decrease in the value of HV to 60.

It is clear by now that limited research, if exists, was conducted for the optimization of FSBE's process parameters in addition to the use of different cooling mediums in the Submerged FSBE (SFSBE) process.

Chapter 3. Methodology

In this chapter, the use of optimization in FSBE's process parameters besides the variously cooled FSBE experimentations are proposed relative to other SPD processes with AZ31-B alloy as the test material.

3.1. Problem Formulation

Since the literature lacks a detailed analysis for the mechanical properties and production indicators of FSBE tubes, a DOE method will be implemented for various process parameters levels as such a process is considered to be new. FSBE will also be explored through experimentations under liquid water-cooling medium to further understand its behavior and grain structure under the effect of multiple cooling rates.

3.2. RSM Optimization

A minimum number of experiments are usually sought with enough information for modeling the response as a function of the process parameters. Fitting and analyzing response surfaces are greatly influenced by the choice of the experimental design. Among the CCDs, FCC is chosen that is considered to be most commonly used with RSM experimental plans. Although CCC provides relative high accuracy compared to face centered CCD, but it requires more level settings per independent variable and used where two or more extremities are inoperable. This is not the case with FCC as it has low and high design levels in its region of interest coinciding with the region of operability making it the simplest response surface design. FCC includes three types of points, Full Factorial (FF), face centered or Axial points and Center points (CP).

Since the case of face centered CCD is present, 3 design levels are required per factor. The design space, represented by a rectangle (Figure 6), is defined using two variables, Feed Rate (f) with a range of 60-120 mm/min and Rotational Speed (N) with a range of 1400-2000 rpm. While the FF points are placed at the corners of design space, star points are placed in the middle of the boundary edges of the design region (points on a circle of radius $\alpha = \pm 1$) as shown in Figure 6 and the CP is in the center of the design levels. Alpha of 1 indicates a rotational speed/feed rate of 2000 rpm or 120 mm/min and vice versa for alpha of 0 and -1. The total number of experiments required in this 2-D design space is a maximum of 13 (4 FF, 4 Axials, and 3-5 CPs depending on the situation). The data points for the two-level FF is 2^k which gives a value of 4,

the number of star points is 2k which is 4 given that k = 2 while CP are maximized to be 5 summing it all up to 13 experimentations. The design space settings are selected based on the literature and the operational capabilities of CNC milling machine.

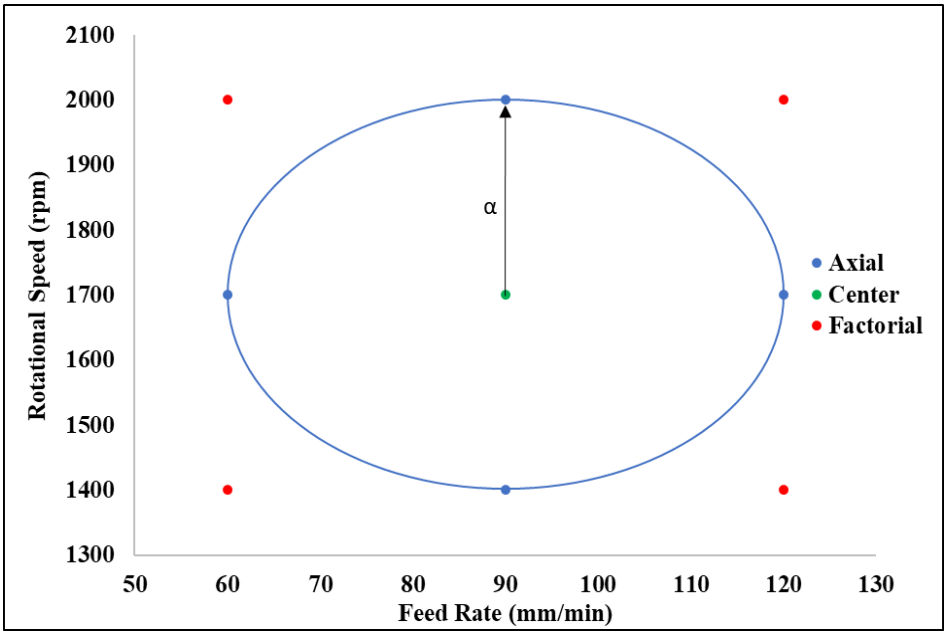

Figure 6: Face centered CCD design space

3.2.1. Mathematical model construction. Since the mathematical relationship between the inputs and outputs is said to be nonlinear based on behavior of the response variables, a modeling technique such as second order polynomial regression is used to describe the output response as a function of the process input variables. The quadratic polynomial model (y) can be represented in Equation 1 [13]:

$$y = \beta_o + \sum_{i=1}^{k} \beta_i x_i + \sum_{i=1}^{k} \beta_{ii} x_i^2 + \sum_{i<j} \sum \beta_{ij} x_i x_j + \epsilon \quad (1)$$

And for the two used factors, selected polynomial regression of degree 2 is expressed in Equation 2 [13]:

$$y = \beta_o + \beta_1(f) + \beta_2(N) + \beta_{11}(f^2) + \beta_{22}(N^2) + \beta_{12}(fN) \quad (2)$$

where β_o, β_1, β_2, β_{11}, β_{22} and β_{12} are the regression model coefficients

3.2.2. Desirability function construction. The output mathematical models of the responses are used along with constraints dictated by the range and physical nature of process parameters to find the optimal settings. The desirability function approach is one of the most frequently used multiple-responses optimization techniques

in practice due to its simplicity and efficiency [14,76]. The method makes use of an objective function *D* called the composite desirability function and transforms each individual response into scale free value (d_i) called individual desirability. Both *D* and d_i desirability ranges from zero (least desirable) to one (most desirable) as a value of one indicates the achievement of desired objective. Mathematically, composite desirability *D* can be defined in Equation 3 [13]:

$$D = (d_1 \times d_2 \times d_3 \times \ldots \times d_n)^{\frac{1}{n}} = (\prod_{i=1}^{n} d_i)^{1/n} \quad (3)$$

Individual desirability d_i has different forms depending on response objective as shown in Equations 4-6 [13]:

Goal is to maximize $f(1)$

$$d_1 = \begin{cases} 0 & f(1) < L_1 \\ \left(\frac{f(1)-L_1}{H_1-L_1}\right)^{w_{t1}} & L_1 \le f(1) \le H_1 \\ 1 & f(1) > H_1 \end{cases} \quad (4)$$

Goal is to minimize $f(2)$

$$d_2 = \begin{cases} 1 & f(2) < L_2 \\ \left(\frac{H_2-f(2)}{H_2-L_2}\right)^{w_{t2}} & L_2 \le f(2) \le H_2 \\ 0 & f(2) > H_2 \end{cases} \quad (5)$$

Goal is to set $f(3)$ to target *T*

$$d_3 = \begin{cases} \left(\frac{f(3)-L_3}{T-L_3}\right)^{w_{t31}} & L_3 \le f(3) \le T \\ \left(\frac{H_3-f(3)}{H_3-T}\right)^{w_{t32}} & T \le f(3) \le H_3 \\ 0 & otherwise \end{cases} \quad (6)$$

where L_i and H_i are lower and upper bound of response, *f(i)* is mathematical model, and w_{ti} is a weight factor range from 0.1 to 10 and controls the shape of the desirability function. For example, if $w_{ti} = 10$ for a specific response then this response is 10 times more important than other responses, whereas for a value of 1, the individual desirability d_i will vary from 0 to 1 in a linear fashion. For the conducted analysis, and without any general loss, the weight factor will be assumed one for all responses. Considering all *n* responses, clearly one wishes to choose the settings for process

parameters to maximize *D*. A value of *D* close to 1 implies that all responses are in a desirable range simultaneously.

3.3. Experimental Investigation

The experimental design plan conducted using three stages. First, FCC experiment is carried out to explore an initial region where *N* ranges from 1400 rpm to 2000 rpm and *f* from 60 mm/min to 120 mm/min. The experimental runs are represented by the solid circles in Figure 7 while design region is represented by the upper left solid line rectangle. The values in Figure 7 are the UTS and toughness values per experiment. As mentioned earlier, 13 experiments formed the initial FCC experiment, but there was a need to explore a wider region especially at higher *f* and lower *N*. This was deduced through the method of steepest ascent. Such a method implements a procedure considering the increment up the ladder in the direction of the maximum increase of a given response (minimum decrease in steepest descent). As a result, the wider range extended *f* to an upper level of 150 mm/min while N to 1000 rpm which concerns the addition of 6 experiments. The direction was chosen in a tradeoff scenario between the outputs which means that it was not solely based on a single response although the priority was for the UTS. The extended experimental layout is represented by the dashed rectangle shown in Figure 7.

Finally, the response models were validated using additional points to investigate model prediction error. The first set of 2 validation points are represented by triangles in Figure 7. The prediction error was significant therefore, it was decided that the former validation points are to be included in the DOE and a new set of validation point are extracted and depicted as X in the same figure. In this way, the optimal settings were validated and the model's error was analyzed.

3.3.1. Tensile testing. Tubular dog bone samples are machined from the extruded tubes in order to conduct uniaxial tensile tests to obtain the mechanical properties. The tests were conducted at room temperature with a crosshead speed of 0.1 mm/sec.

3.3.2. ANOVA and optimization. The mechanical properties besides the productivity indicators are analyzed through ANOVA in Minitab in which each model's term is considered significant if its P-value is less than or equal to the significance level

of 0.1. In other words, a maximum of 10% chance is allowed for the outputs to have random values and change due to nothing related to the experiment. The responses will be further used to develop mathematical models for the response variables. Afterwards, the optimal settings of FSBE using desirability multi-response optimization technique are found twice. Optimal process conditions that maximize the mechanical properties only, then include Cycle Time (CT) and Power consumption (P) and find optimal settings that improve mechanical properties and minimize power and cycle time.

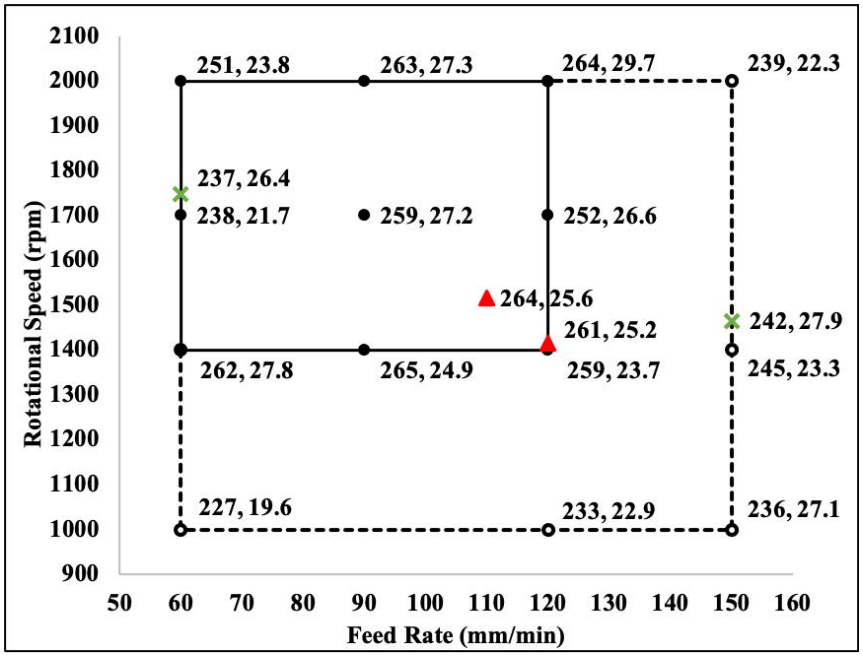

Figure 7: Experimental plan layout

3.3.3. Submerged FSBE. Experiments with different cooling methods conducted at specific process parameters, 2000 rpm and 90 mm/min, for AZ31-B alloy. The experimentations are divided into naturally cooled, cold water cooled and room temperature cooled methods where 2 experiments are conducted per medium for the consistency of results without the need for a third test since the stress strain curves were very close to each other. The temperature and power measurements were recorded for each experiment.

Chapter 4. Experimental Setup

This chapter discusses the different testing procedures of FSBE and tensile. With the material used being AZ31-B alloy shaped as rods, a thorough explanation of the setups exists highlighting the design and measurement techniques of power and temperature besides the mechanical properties.

4.1. Material

AZ31-B magnesium wrought alloy is used in the FSBE experimentations having a chemical composition as stated in Table 1 and it is bought from Aircraft Materials, United Kingdom. The AZ31-B alloy rods are received with a height and diameter of 180 cm and 2.54 cm, respectively. Turning process is implemented to reduce the cylindrical billet's diameter to 19 mm with a height of 50 mm.

Table 1: Chemical Composition of AZ31-B (wt. %) [77]

Al	Zn	Mn	Si	Cu	Ca	Fe	Ni	Others	Mg
2.5 -3.5	0.7 -1.3	0.2 min	0.05 max	0.05 max	0.04 max	0.005 max	0.005 max	0.3 max	remaining

4.2. Testing Equipment

4.2.1. FSBE setup. FSBE tests are conducted using a three-axis DOOSAN DNM 4500 vertical CNC machining center with a maximum spindle speed of 8000 rpm where Figure 8 depicts the manufacturing setup. The stirring tool used is 4037 steel alloy with 19 mm in diameter with a 10° tapered and filleted head to ease material penetration. The extruding dies are prepared from 4140 steel alloy and made into two halves with a die cavity of 19.05 mm in diameter. The die cavity is drilled after fixing both dies together to ensure that the axisymmetric condition is met. Two setscrews from different sides are used at the bottom of the dies to prevent the initial sample rotation at the onset of contact due to the spinning of the puncher. In order to measure temperature during the extrusion process, three small holes are drilled in the die and type K thermocouples are mounted at top, middle and bottom of die. Temperature measurements are recorded using Pico TC-08 thermocouple data logger. All experiments are conducted in a dry environment while varying spindle speed and axial

feed rate. The FSBE test begins as the puncher dives through the cylindrical specimen at a given *f* and *N* for 45 mm leaving 5 mm at the tube's bottom in order to maintain a safe distance between the formed tube and the cavity's bottom surface. Since the temperature can rise to temperatures greater than 200 °C during the test due to self-induced heat generation, three extrusion dies were prepared so that three runs can occur in succession. During the tests, instantaneous power and cycle time readings were recorded using the 3-phase PS2500 power logger. To ensure test repeatability, the stirring tool and the extrusion dies cavity are slightly polished and honed, respectively after each test.

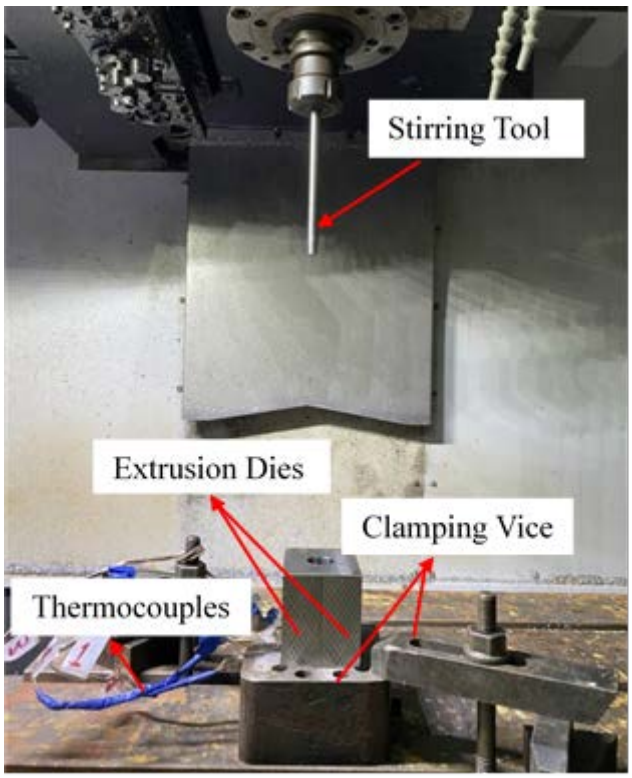

Figure 8: FSBE experimental setup

As a matter of fact, the SFSBE fixture is quite similar to Figure 8, however the extrusion dies are firmly placed amid the properly sealed galvanized iron box with a steel base and an open top (Figure 9). The box's dimensions are 265 mm, 225 mm and 200 mm with regard to the length, width and height, respectively. The water is levelled up to 3-4 cm above the top surface of the extrusion dies to ensure that they are fully immersed. For the cold-water experimentations, big chunks of ice were added to the tap room temperature water as implied in Figure 9 to cool it down for a temperature around

2 °C meanwhile the Mg billet is already placed in the die opening. Similar to the air-cooled experiments, temperature and power readings will also be recorded during the FSBE process using the previously mentioned equipment.

Figure 9: SFSBE Setup

4.2.2. Tensile test setup. Uniaxial tensile tests are conducted to obtain mechanical properties such as UTS, toughness and % elongation. Since the AZ31-B processed tubes' results in a rough surface finish due to the induced heat, tube diameter is reduced by 1 mm using turning in addition to reaming the bore diameter. The extruded tube will also be reduced in height of 5-6 mm from the bottom to eliminate the tapered section besides the reduction of 2 mm as well from the top to remove the ring section. Afterwards, the extruded tubes are machined to get a dumbbell shape specimen as shown in Figure 10a. Since the workpiece is curved, sharp corners around the rear surface are sanded to achieve a smooth surface finish to prevent stress concentration points that can cause early fracture. Finally, the dog bone sample (Figure 10b) is spray-painted with white colour to create a clear uniform background then it is sprayed with black to have a speckle pattern. Tensile tests are performed using Instron universal testing machine model 5982 equipped with 3D DIC setup shown in Figure 11 to capture surface deformation from two directions as the specimen is curved.

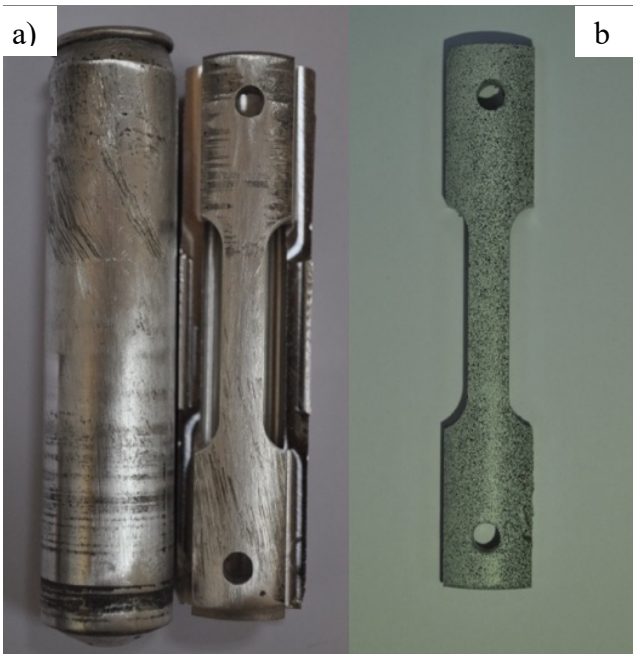

Figure 10: a) shows the extruded tube and after its CNC machined b) dumbbell specimen

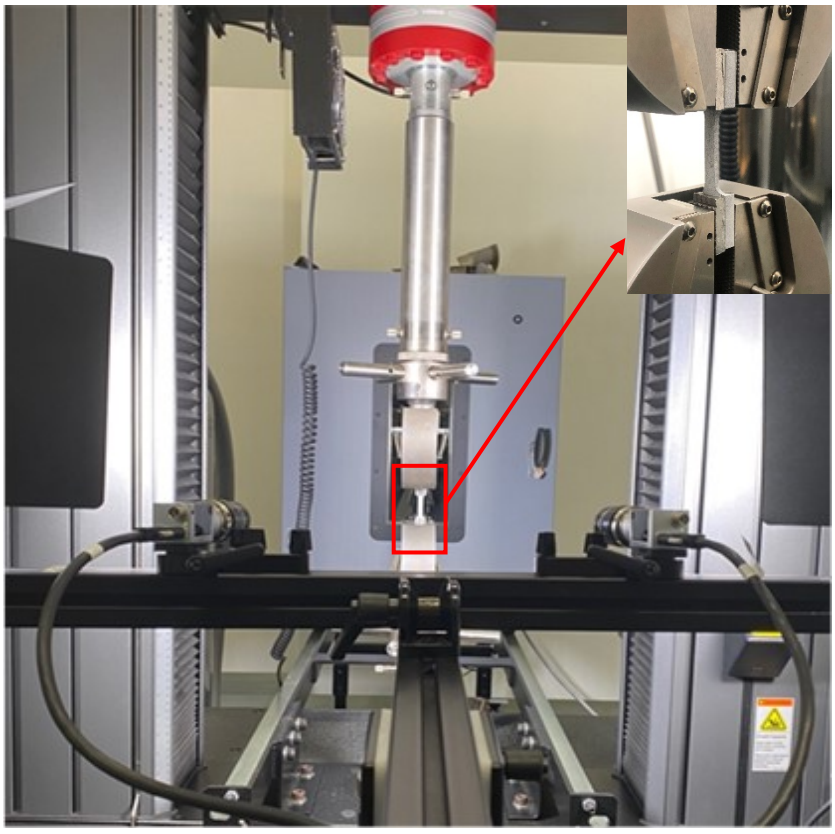

Figure 11: Tensile setup with 3D DIC system

Chapter 5. Results and Discussion

The work presented in this chapter aims at exploring the outcomes of the optimization of FSBE process through RSM desirability multi-response optimization technique and the specimens' mechanical behavior extruded through different axial feed rates and rotational speeds. ANOVA tables and contour plots are presented for some of the mechanical properties and production parameters. In addition, several stress strain curves are presented to graphically show the gap of many mechanical properties such as UTS among differently processed samples. Temperature and power consumption profiles are shown to understand the material's behavior across the differently cooled tubes besides microstructure characterization.

5.1. RSM Optimization of FSBE

Results of experimental plan are summarized in Table 2 while a sample of the modified stress strain curves under different f and N conditions are depicted in Figure 12. The curves selected represent conditions resulted in lowest, average and highest UTS. The range of UTS extended from 233 MPa to 265 MPa which is considered statistically significant difference when compared to general error of experiment. For the sake of investigating the impact of process parameters on mechanical and production properties of FSBE process, each response is modeled and plotted using contour plots. RSM mathematical models are summarized in Equations 7-10 using coded factors along with coefficient of determination, R^2, which provides an estimate of goodness of fit while the ANOVA tables are presented in Tables 3-7. In other words, the R^2 is a statistic ranging from 0 to 1(100%) used to provide an indication about the reduction in variability of a given response model and how well can future results be close to that model. The coded equations are presented instead of the actual models as they provide an indication about which terms in a given model are significant through their coefficients' values, so the higher the coefficient the more important the term is. The UTS's R^2 of 71 suggests that 71 % of experiments variability is explained by the model suggested in Equation 7. The remaining variability in the prediction power can be traced to the use of CNC machine operation for extrusion in addition to the use of measurement devices for the mechanical properties and power consumption. It is known that variations exist in the mechanical properties due to the nature of the material as well as the sample preparation using the CNC machine which is not a consistently

accurate procedure that greatly adds to the induced variability. The possible use of wire cut electrical discharge machining can highly reduce the variability as it is quite accurate in the tube preparation process. On the other side, the measurement technique for the cycle time was only through a stopwatch timer thus, it shows a high prediction power.

Although UTS, toughness, P and CT showed significant change due to variation in *f* and *N*, % elongation did not. % elongation ranges from 9.58 % to 11.67 % which has a 22 % difference between the minimum and maximum. This difference is very close to the error, the difference between the highest and lowest values given the repeatability of the same experiment. Having an adj MS (Mean Square) value of 0.611 for the model and an adj MS error of 0.713 indicates an F-value of 0.86 (ratio of 0.611 by 0.713). As both MSs are very close to each other and having an approximate F-value of 0.9, 90 % of the difference in the model is from the error. Apparently, this difference is not because the change of variables, but due to happening by chance. As the F-value represents the ratio of both means, having a value less than or equal to 1 (the variable's adj MS is less than the MSE) implies that % elongation is not statistically significant when compared to 0.9 of the experiments' MSE. Regarding the other properties, a much higher F-values exits for their models which proves their significance. For example, UTS's mathematical model has an F-value of 6.5 which means that the model's effect is almost 7 folds more than the error.

Table 2: DOE Results

Test	Process Parameters		Responses				
	Rotational Speed	**Feed Rate**	**UTS (MPa)**	**% EL (%)**	**Toughness (J/m^3)**	**P (kW)**	**CT (sec)**
1	1400	120	259.53	9.58	23.73	163.70	24.0
2	1700	120	252.20	11.28	26.58	113.77	25.0
3	1700	90	265.42	11.62	29.34	135.15	31.0
4	1700	90	262.89	11.08	27.71	135.87	32.0
5	1700	90	263.07	10.74	25.67	129.86	31.0
6	1700	90	262.86	10.83	26.20	125.85	31.0
7	1700	90	259.06	10.08	27.23	131.27	32.0

8	2000	120	264.94	11.67	29.70	112.76	25.0
9	2000	60	251.31	9.99	23.75	174.22	47.0
10	1400	90	265.47	9.92	24.96	128.27	32.0
11	1700	60	238.94	9.52	21.73	238.91	45.5
12	1400	60	262.22	11.12	27.67	172.00	47.0
13	2000	90	263.12	10.80	27.32	131.82	31.0
14	2000	150	239.43	9.89	22.32	114.98	18.5
15	1000	150	236.22	11.91	27.06	95.53	19.0
16	1400	150	245.63	9.99	23.27	91.27	19.0
17	1000	60	227.76	9.02	19.58	161.61	46.0
18	1000	120	233.48	10.33	22.92	101.66	23.0
19	1465	150	242.45	12.07	27.88	140.19	19.0
20	1748	60	237.38	11.58	26.39	248.62	46.0
21	1516	110	264.32	10.19	25.59	170.76	24.5
22	1414	120	261.56	10.11	25.18	161.60	23.0

$$UTS = 262.8 + 7.41N - 9.36N^2 - 16.16f^2 \ \ (R^2 = 71\%) \quad (7)$$

$$Toughness = -6.9 + 0.012N + 0.394f - 0.0112f^2 - 0.00008Nf \ \ (R^2 = 63\%) \quad (8)$$

$$P = 138.37 - 36.92f - 28.1N^2 + 30.8f^2 \ \ (R^2 = 61\%) \quad (9)$$

$$CT = 89.56 - 0.897f + 0.00285f^2 \ \ (R^2 = 99\%) \quad (10)$$

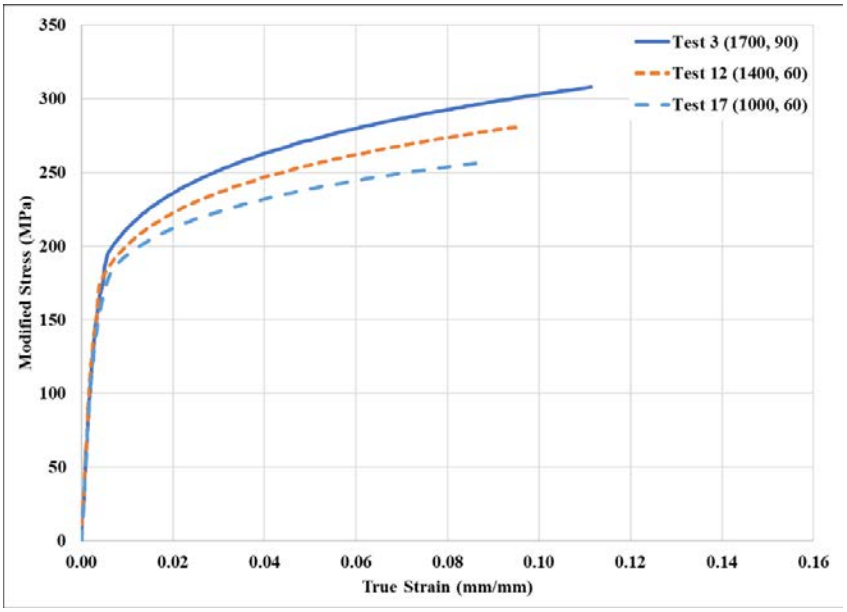

Figure 12: Modified stress strain curves

Figures 13 and 14 show the three-dimensional RSM plot and contour plots for the toughness and UTS, respectively in terms of *f* and *N*. Since only 2 controllable variables exist, it is applicable to find the stationary point from the responses surface plots however for more than 2 factors numerical methods are to be used. Curved contours can characterize the response surface and locate the optimum location with respect to axial feed rate and spindle speed. This optimum is referred to as a stationary point (slope is zero) where it can be maximum, minimum or a saddle point. It is clear through the response surface plots whether the contour is concaved up, down or represents a minimax. Response surfaces and contour plots in the UTS and toughness demonstrate the nonlinear effect of *f* and *N* on responses represented by the quadratic and interaction terms in Equations 7-8.

UTS contour plots suggests that UTS increases as *N* and *f* increases until a certain value, roughly 1700 rpm and 105 mm/min, then UTS start to decrease. Toughness plots suggests similar behavior in terms of feed rate only. In terms of rotational speed, toughness is directly proportional to it so as the spindle speed increases the toughness will increase. As a result, the maximum UTS can be achieved by setting *N* and *f* at 1700 rpm and 105 mm/min while maximum toughness can be reached by a combination of *N* and *f* at 2000 rpm and 96 mm/min, respectively. This could be attributed to the relationship between UTS and toughness. Toughness is the energy stored in the material until fracture (failure) or the area under stress-strain curve, which is driven by UTS and % elongation. Since the % elongation change is not significant, toughness will mainly follow UTS's behavior.

Table 3: UTS ANOVA

Source	DF	Adj SS	Adj MS	F-Value	P-Value
Model	5	2012.14	402.428	6.50	0.004
Speed	1	476.15	476.154	7.69	0.017
FR	1	29.37	29.371	0.47	0.504
Speed* Speed	1	319.91	319.912	5.17	0.042
FR*FR	1	502.15	502.147	8.11	0.015
Speed*FR	1	19.01	19.012	0.31	0.590
Error	12	742.69	61.891		
Lack-of-Fit	8	721.85	90.232	17.32	0.007
Pure Error	4	20.84	5.210		
Total	17	2754.83			

Table 4: Percent Elongation ANOVA

Source	DF	Adj SS	Adj MS	F-Value	P-Value
Model	5	3.059	0.611	0.86	0.536
Speed	1	0.197	0.197	0.28	0.609
FR	1	0.725	0.725	1.02	0.333
Speed*Speed	1	0.041	0.041	0.06	0.813
FR*FR	1	0.832	0.832	1.17	0.301
Speed*FR	1	1.025	1.025	1.44	0.254
Error	12	8.561	0.713		
Lack-of-Fit	8	7.311	0.914	2.93	0.157
Pure Error	4	1.249	0.312		
Total	17	11.620			

Table 5: Toughness ANOVA

Source	DF	Adj SS	Adj MS	F-Value	P-Value
Model	5	81.217	16.2435	4.11	0.021
Speed	1	13.007	13.0066	3.29	0.095
FR	1	5.835	5.8349	1.48	0.248
Speed*Speed	1	0.075	0.0754	0.02	0.892
FR*FR	1	36.416	36.4161	9.21	0.010
Speed*FR	1	11.679	11.6788	2.95	0.111
Error	12	47.440	3.9534		
Lack-of-Fit	8	39.291	4.9114	2.41	0.206
Pure Error	4	8.149	2.0372		
Total	17	128.658			

Table 6: Power ANOVA

Source	DF	Adj SS	Adj MS	F-Value	P-Value
Model	5	14870.7	2974.14	5.55	0.007
Speed	1	362.7	362.70	0.68	0.427
FR	1	9821.4	9821.36	18.33	0.001
Speed*Speed	1	1114.0	1114.02	2.15	0.105
FR*FR	1	2358.0	2358.03	4.40	0.058
Speed*FR	1	21.2	21.21	0.04	0.846
Error	12	6428.6	535.71		
Lack-of-Fit	8	6361.5	795.19	47.45	0.001
Pure Error	4	67.0	16.76		
Total	17	27299.3			

Table 7: Cycle Time ANOVA

Source	DF	Adj SS	Adj MS	F-Value	P-Value
Model	5	1564.48	312.90	250.88	0.000
Speed	1	0.01	0.01	0.01	0.917
FR	1	1344.44	1344.44	1077.97	0.000
Speed*Speed	1	0.01	0.01	0.01	0.921
FR*FR	1	95.44	95.44	76.52	0.000
Speed*FR	1	0.08	0.08	0.06	0.809
Error	12	14.97	1.25		
Lack-of-Fit	8	13.77	1.72	5.74	0.055
Pure Error	4	1.20	0.30		
Total	17	1579.44			

As earlier stated, the F-value is a ratio of the factor's adj MS value by the error's adjusted MS value. Values that are way larger than 1 such as, the power's model MS, shows that the variable's MS is higher than MSE and further indicates that the variation or difference is not happening by chance as the comparison between the means is legitimate. It also indicates that the null hypothesis is rejected and vice versa for F-values of equal magnitude or less.

Another value to decide the statistical significance of a response is through the P-value. It can be observed that some terms in each model are having a P-value more than 0.1 (10 %) which is the set threshold; therefore, they are not included in the mathematical model as they are not statistically significant. However, very close P values to 0.1 can be accepted as they might have a significant impact of the model's prediction power such as the 2-way interaction term (0.111) in the toughness. The idea of threshold is greatly enforced in the % elongation as its model as a whole has a P-value of 0.536 implying that the predicted values have 53.6 % chance of being random (happened by chance) or that they are not triggered by any reason in the experiments. Another example would be the rotational speed's linear term in the power response. It has a P-value of 0.427 >> 0.1; hence, it was not included in the power model. In the case of exceeding the threshold, the null hypothesis is accepted while the alternative hypothesis is rejected and vice versa [13]. In other words, the null hypothesis is when there is not a direct effect of a term on the response or it can also be referred to when the output variable is not being influenced by the change in the input variable(s). This is the case with the effect of f and N on % elongation.

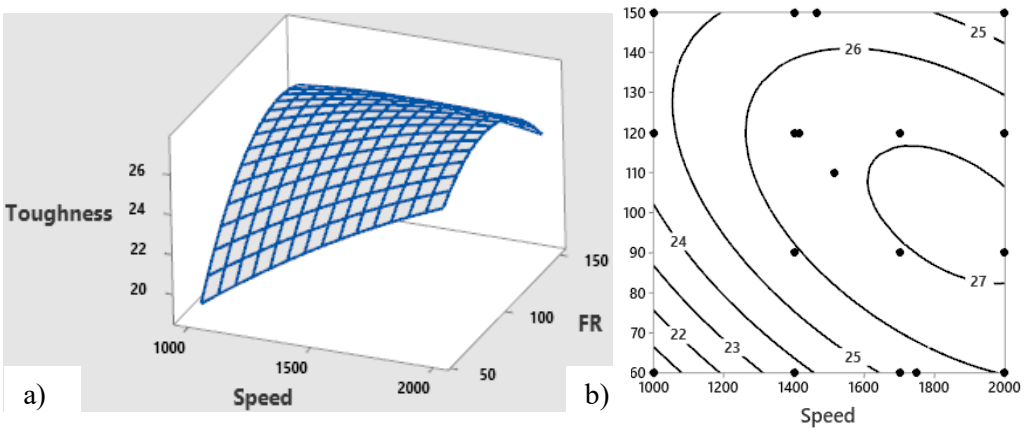

Figure 14: a) Toughness RSM and b) Contour plot

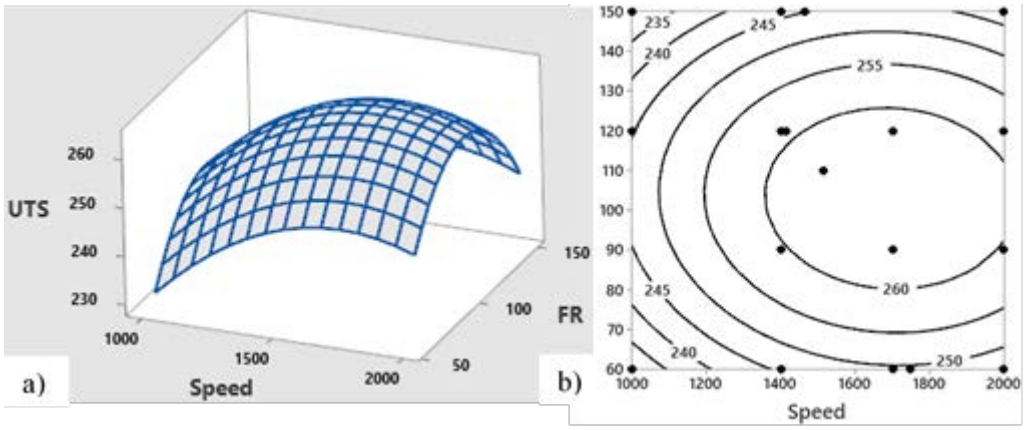

Figure 13: a) UTS RSM and b) Contour plot

Figures 15a,b and 16a,b depict the response surfaces and contour plots of power consumption and cycle time, respectively. One can clearly note that the cycle time is a function of only one process parameter, feed rate, while power is influenced by both parameters. Power increases as rotational speed increases, then decreases around 1600 rpm. In terms of the axial feed rate, power decreases as feed rate increases.

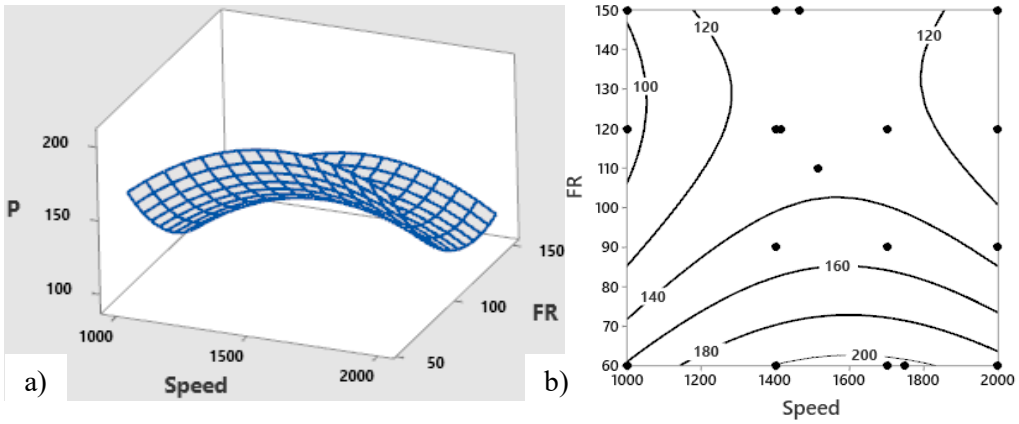

Figure 15: a) Power Consumption RSM and b) Contour plot

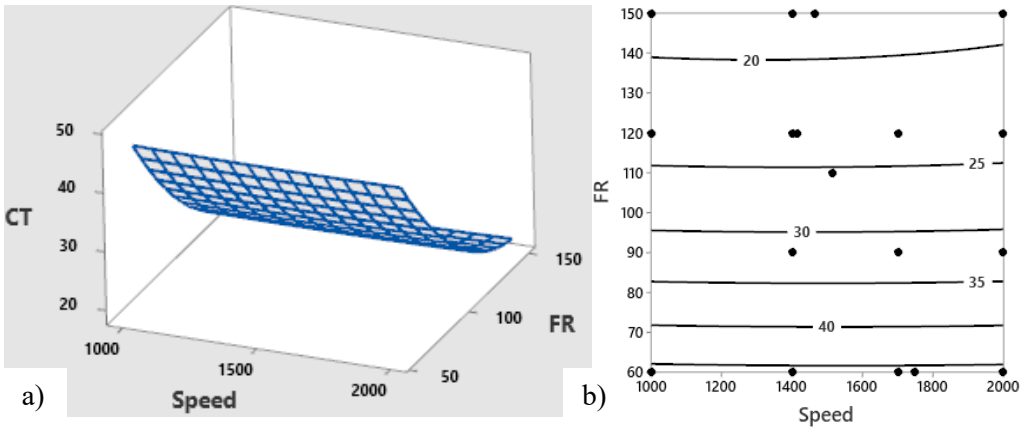

Figure 16: a) Cycle Time RSM and b) Contour plot

From the examination of the UTS contour plot, it is noted that UTS is slightly more sensitive to changes in *N* than to *f*. This is due to the gap distances between the contours in both directions as the contours are not purely circular in fact, they resemble a horizontal oval shape. Therefore, the gap between the contours through the descent from the peak value in the horizontal direction (rotational speed) increases more than in the vertical direction (feed rate). Another way of finding the factor that is more sensitive than the other with respect to a certain output is through the use of canonical analysis [48]. Such method is conducted where the canonical form is represented in Equation 14 [13]. However, starting with second order model expressed in Equation 11:

$$\hat{y} = \hat{\beta}_0 + x'b + x'Bx \tag{11}$$

where *x*, *b* and *B* are in matrix notation which are the independent variables and linear regression coefficients, respectively while *B* is a symmetric matrix with the trace being the quadratic coefficients are the off diagonals are the interaction terms.

$$x = \begin{bmatrix} x_1 \\ x_2 \end{bmatrix} \quad b = \begin{bmatrix} \hat{\beta}_1 \\ \hat{\beta}_2 \end{bmatrix} \text{ and } B = \begin{bmatrix} \hat{\beta}_{11} & \hat{\beta}_{12}/2 \\ \hat{\beta}_{12}/2 & \hat{\beta}_{22} \end{bmatrix}$$

Equation 12 represents Equation 11 after equating it to zero (derivative is zero) and then solving for *x* (stationary point):

$$b + 2Bx = 0 \xrightarrow{solving\ for\ x} x_s = -\frac{1}{2}B^{-1}b \tag{12}$$

Substituting *x* in Equation 11:

$$\hat{y}_s = \hat{\beta}_0 + \frac{1}{2}x_s'b \tag{13}$$

Canonical form of a response model is illustrated in Equation 14:

$$\hat{y} = \hat{y}_s + \lambda_1 \omega_1^2 + \lambda_2 \omega_2^2 + \cdots + \lambda_k \omega_k^2 \quad (14)$$

where (λ_i) are characteristic roots (eigenvalues) of the matrix β and (ω_i) are the transformed design factors (canonical variables).

The eigenvalues are scalers used to transform the eigenvectors from the original equations (coded mathematical models). This results with the above stated transformed fitted model with the stationary point as its origin having transformed (rotated) axes of ω_1 and ω_2. Such eigenvalues are obtained by solving the roots of Equation 14 through a MATLAB code (Appendix A) except cycle time as it is only influenced by feed rate. Based on this analysis, two eigenvalues corresponding to *N* and *f* respectively, λ_N and λ_f, are obtained and used to indicate sensitivity strength. The response surface's shape can be further clarified through the signs and absolute values of the canonical model's coefficients besides the stationary point. Positive eigenvalues show that the stationary point is a point of maximum and vice versa for negative eigenvalues. On the other hand, mixed signs indicate the presence of a saddle point. For example, the roots of the UTS canonical quadratic equation are $\lambda_N = -16.16$ and $\lambda_f = -9.36$. Since both are negative, the stationary point is the maximum response. Given that $|\lambda_N| > |\lambda_f|$, this confirms that UTS is more sensitive to changes in rotational speed than feed rate which agrees with the respective surface plot in Figure 13a. Similarly, distances between contour curves and eigenvalues for toughness indicates that toughness is also more sensitive to changes in spindle speed than axial feed rate.

Furthermore, the mathematical models were verified by analyzing the residual points (ϵ) and their plots which resulted in normally distributed residuals with the predicted and experimental values averaged out to be zero being very close to the 50th percentile. The 50th percentile in the normal probability plot indicates that some residuals are of negative sign and some of a positive sign. In addition, the variance is constant in the versus fits. Such residual plots are shown in Figure 17 which represents the case of the UTS response variable. The residual plots for the other uncontrollable responses are found in Appendix B.

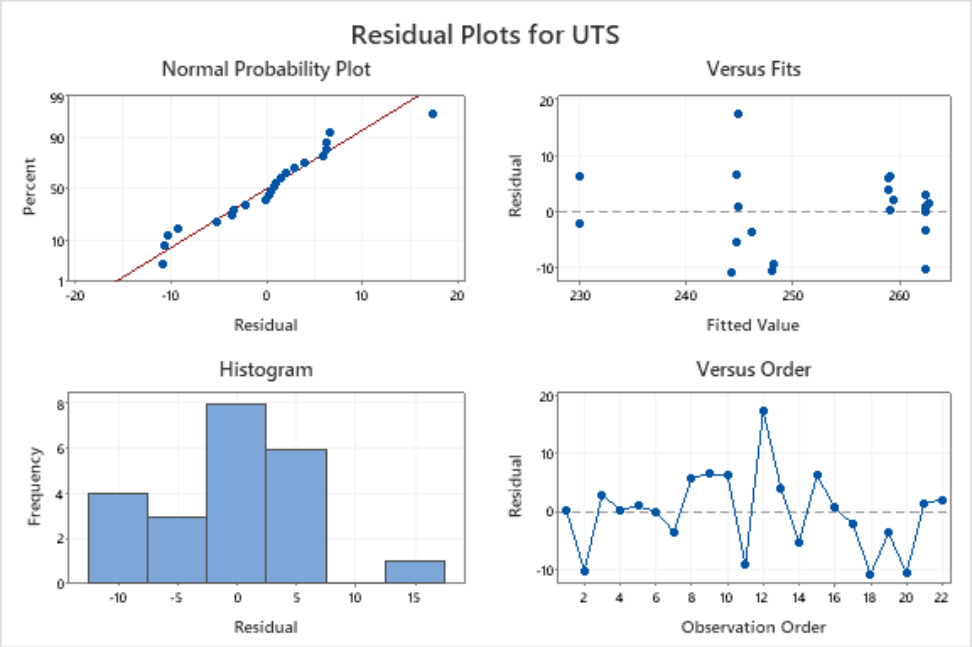

Figure 17: UTS's residual plots

Hot and cold working processes operate above and below the material's recrystallization temperature, respectively. The recrystallization temperature is the minimum required temperature, 30-60 % of the melting point, for the deformed material to form new grains which is approximated to be 350 °C in Mg AZ31 alloy according to Wang et al. [78]. However, this is not the case with FSBE processed material, as it goes through heating and strain hardening simultaneously. Recovery, recrystallization and grain growth are the three physical processes that occur in succession during FSBE on the microstructural level [79]. Recovery is defined as the drop in the dislocation density in the grain structure due to the removal of linear defects by annihilation besides their rearrangement as they begin to move to different planes at a high temperature reducing the grains internal stored strain energy [7]. Dynamic recovery is the occurring phenomena as the respective bulk extrusion operates under high temperature and plastic deformation conditions. The high initial strain stored initiates the nucleation of fine strain free and equiaxed grains in a process described as recrystallization. Such newly formed grains grow until they consume the deformed strained grains for a certain time at high strain energy sites with inhomogeneities such as high angle grain boundaries. Similarly to dynamic recovery, dynamic recrystallization describes the current situation as it happens meanwhile material deformation with thermal input [80]. The strength of the friction stir processed material depends mainly on grain size as finer grains result

in improved strength. The recrystallization rate is greatly influenced by two main factors, temperature and time (Figure 18). High heat input after sufficient recovery and recrystallization results in the undesirable process referred to as grain growth. Such a process induces grain coalescence as the small grains continue to grow and merge together which outcomes in the reduction of the grain boundary energy stored in the microstructure as the number of grains are less. Grain growth will have a negative impact on the mechanical properties that cannot be avoided [79].

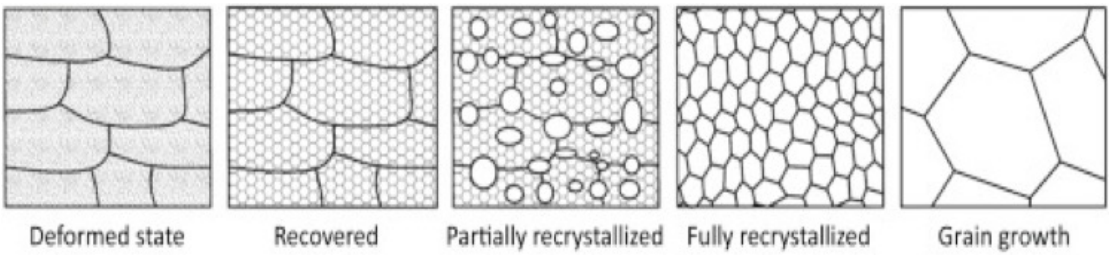

Figure 18: Recovery, recrystallization and grain growth in metallic material [67]

Figure 19 shows the temperature profile with time measured in the middle of the extrusion dies for four different test conditions that include some of the extreme process parameters (highest rotational speed or feed rate and vice versa). The peak temperature in this curve is an indication of heat generated by frictional contact between the workpiece and the stirring tool and due to plastic deformation. As the peak temperature increases, higher heat is supplied to the processed material. The heat input plays a crucial role in determining the final grain size in the FSBE AZ31-B material. If the heat input is too high, significant grain growth will occur after the recovery and recrystallization processes are completed. Rotational speed of 2000 rpm and 60 mm/min feed rate represent this case. If the heat input is too low, insufficient recrystallization and limited plastic flow will result in coarse grains. The two curves in Figure 19 that correspond to 2000 rpm and 150 mm/min and 1000 rpm and 60 mm/min are examples of insufficient heat input. Therefore, very high or very low heat generated have undesirable effects on the extruded seamless tubes. Referring to the mechanical properties, UTS and toughness, results provided in Table 2, the amount of heat generated at 1700 rpm and 90 mm/min will result in fine grains due to sufficient recrystallization and minimal grain growth that improve the previously mentioned properties.

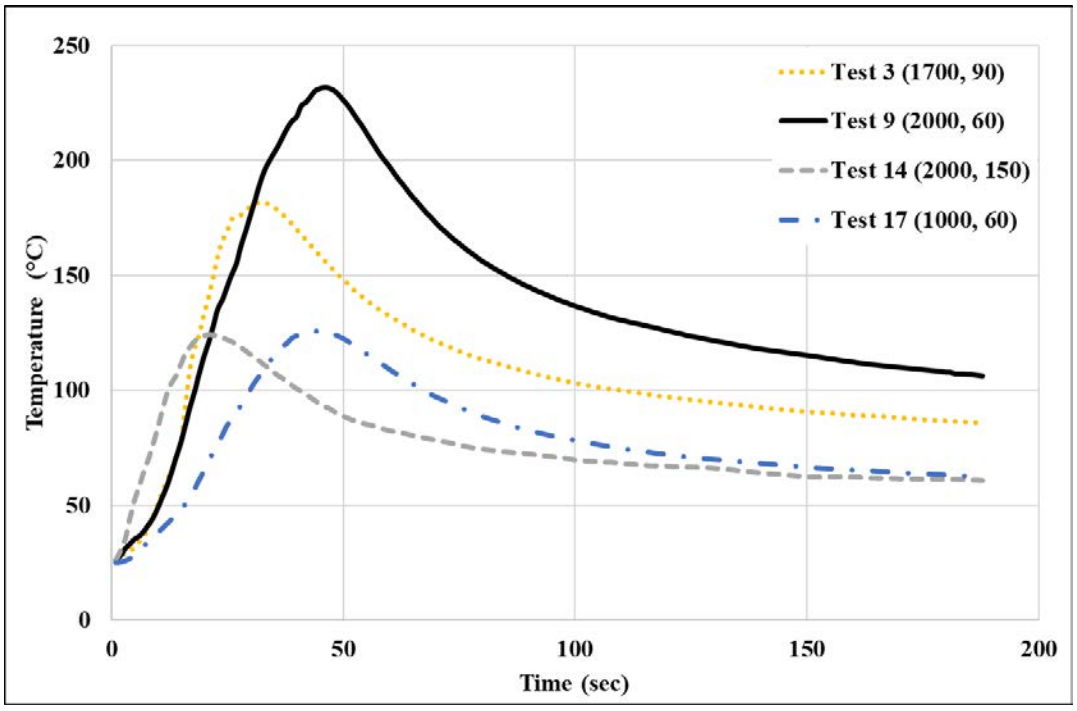

Figure 19: Temperature vs time in the die for different conditions

Using Minitab, the desirability multi-response optimization technique is conducted twice. First, the objective is to maximize all mechanical properties (Figure 20a). In the second step, the objective is to maximize mechanical properties and minimize production indicators, power consumption and cycle time, in Figure 20b. The optimal settings of the former case, assuming all properties have the same weight, is 1767 rpm and 102 mm/min. The optimal settings will result into a UTS of 262.3 MPa, toughness of 26.9 J/m^3. In the latter case, the optimal settings include the rotational speed of 2000 rpm and feed rate of 116 mm/min. The respective optimal parameters for the latter case will end with values of 258.6 MPa for UTS, toughness of 27.4 J/m^3, power consumption of 102.9 kW and cycle time of 23.8 sec. Since percent elongation proved its insignificance (P-value = 0.536) with the change in both rotational speed and feed rate, the value of 10.7 % was obtained through prediction for both optimal settings. The individual desirability d_i indicates the amount of deviation from the individual response optimal value. For example, d of 0.92 for UTS indicates a small deviation from the maximum achieved strength of 265 MPa as a value of 1 shows that it is equal to or higher than the latter value.

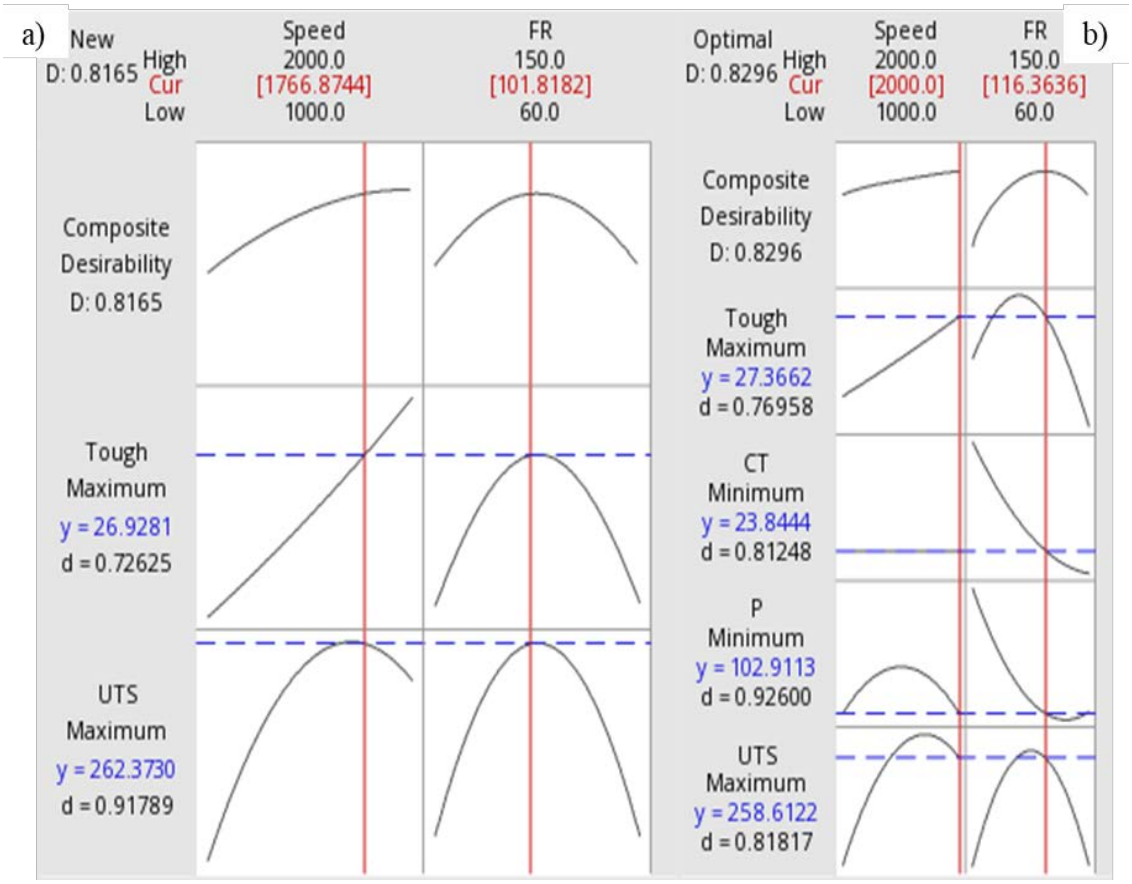

Figure 20: a) Mechanical and b) Overall responses optimization

To validate the optimization results of maximizing the mechanical properties, 2 experiments were conducted at the optimal settings of 1767 rpm and 102 mm/min. The results are summarized in Table 8. The UTS and toughness have an error of 3.1 % and -7 %, respectively. The results variability is of ± 5% for UTS and ± 10% for toughness which are within the measurement's variability and are deemed acceptable.

Table 8: Validation tests

Response	Optimal Predicted	Validation Average	Prediction Error
UTS (MPa)	262.3	270.7	3.1 %
Toughness (J/m^3)	26.9	25.14	-7 %

5.2. Submerged FSBE

The SFSBE process was evaluated through different perspectives including power consumption, mechanical characterization and thermal history. It is well known that the variation in process parameters or cooling rate induce changes in the deformation thermal distribution of SPD process such as FSBE which will consequently result in grain refinement [82,83]. The mechanical properties vary with the change in temperature as it links to the altered microstructure. In the case of SFSBE, each cooling method have distinct specific heat capacity (Cp_{air} = 1.004 kJ/kg·K and Cp_{water} = 4.180 kJ/kg·K) which should induce different mechanical responses. In other words, the ability to absorb the self-generated heat from the extrusion process is not the same throughout.

Two different cooling mediums were implemented, air cooling and water cooling while the latter is divided into room temperature (RT) water and cold water (CW) of 25 °C and 2 °C, respectively. It is noted from the stress strain curves in Figure 21 that changes do occur in terms of UTS and percent elongation however they are statistically insignificant according to the 2 sample T-tests (Appendix C). The T-test is a statistical tool in Minitab that compares the mean of two different data sets to determine the existence of significance. Given that μ_1 is the sample mean of the first group while μ_2 is the sample mean of the second data. The null hypothesis occurs when $\mu_1 = \mu_2$ while the alternative hypothesis is achieved when they do not equate each other as such hypotheses are tested at a significance level of 0.1. For example, UTS in Air compared to UTS in RT (Figure 32a), μ_1 is the average UTS in air while μ_2 is average UTS in RT. In UTS, P-values of 0.1, 0.143 and 0.134 for Air compared to RT, Air compared to CW and RT with CW, respectively. On the other side, percent elongation had P-values of 0.428, 0.634 and 0.243 for the above conditions. Therefore, all of them are greater or equal to the P-value of 0.1 indicating strong evidence for insignificance. In other words, the null hypothesis is accepted. Even though temperature decreases, UTS values started with 263 MPa and resulted in 258 MPa for RT and 262 MPa under CW. Similarly, the percent elongation changes were very minimal from 10.8 % to 10.2 % and 11.5 % for RT and CW. This is relative to SFSW process where the entire workpiece is submerged under a cooling medium while in SFSBE, only the billet's top surface is exposed to the submerged coolant, liquid water. In other words, more surface area is cooled in the former than in the latter and this might explain the invariance in

the mechanical properties as the Mg AZ31 specimen is not being properly cooled. The change in mechanical properties due to the thermal input change from dry cooling to CW and RT with temperatures on the tube's outer diameter of 81 °C and 155 °C starting from 208 °C (Figure 22) which shows a reduction in temperature of around 60 % in the case CW and 25 % in RT.

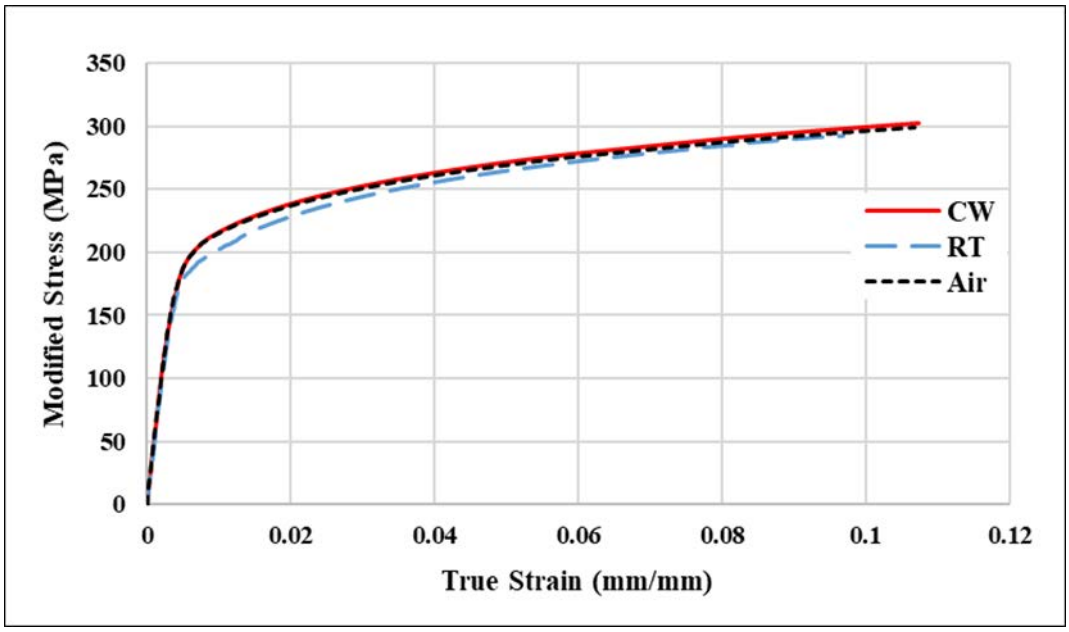

Figure 21: Modified SFSBE stress strain curves

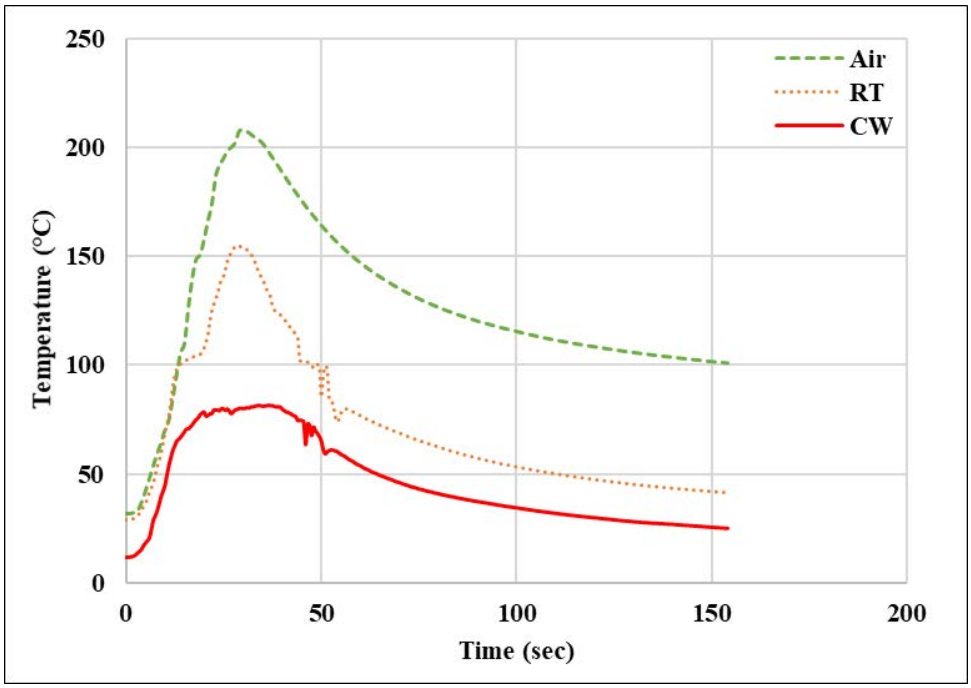

Figure 22: Thermal history across all three cooling mediums

The optical micrographs and grain size distribution plots (Figures 23-26) showed a variation in the grain size across the tube's thickness in all the three samples. Apparently, there exists a strain gradient across the structure's thickness due to the material's behavior in FSBE. The inner zone (wall) had an ultra-fine grain structure due to the combination of high heat input and large strains that results in a series of recrystallization events known as discontinuous dynamic recrystallization.

As previously stated for CW, the measured die temperature is 81 °C which is not quite sufficient for full recrystallization to take place and this is evident from the observed grain size and structure distribution along the circumferential thickness. The smallest average size at the inner wall of 16.8 µm is higher than of the other cooling mediums. Even though air and RT samples presented fine grain structure compared to the above method, they did not present a reasonable difference among themselves. They result in almost the same range of grain size values from 11.5 µm to 12.4 µm.

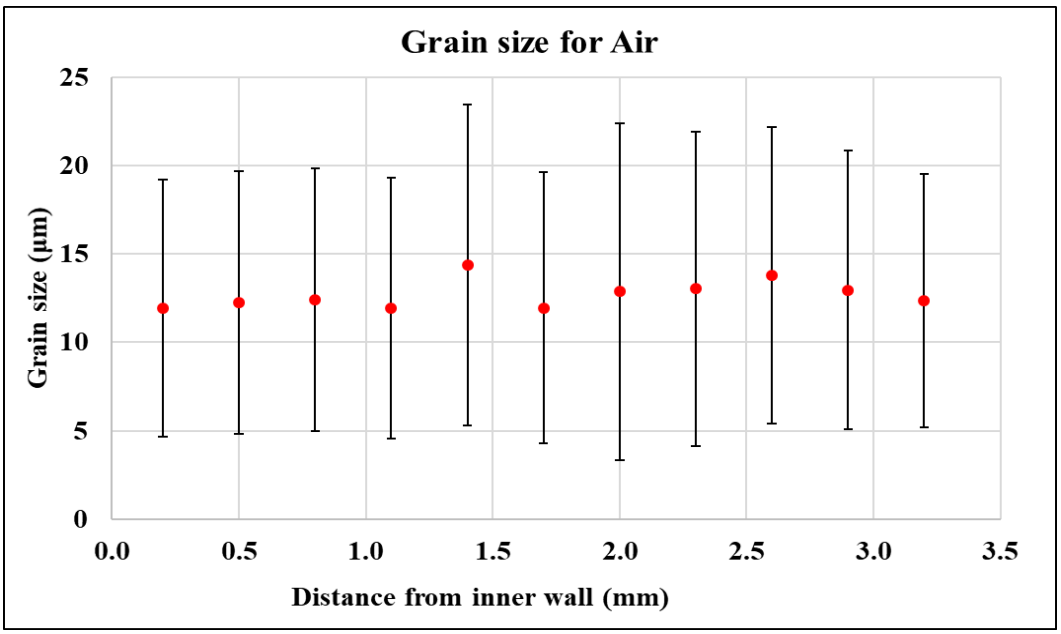

Figure 23: Grain size distribution in air cooled medium

Meanwhile the intermediate zone from 1 mm to 2 mm showed a lower average grain size from 9.8 µm to 11.5 µm in RT (Figure 24) compared with values from 12.0 µm to 14.4 µm in air (Figure 23). This observation besides the drop-in temperature between the above mediums proves that an appropriate recrystallization occurs with very minimal grain growth as the self-generated die temperature of 155 °C is sufficient.

However, that does not indicate the lack of insufficient fine grains in the air-cooled sample, but the effect of grain growth is quite detrimental in such condition as high heat is trapped in the die hole after the end of recrystallization period as much higher temperatures are expected at the tube's inner wall. Additionally, the peak grain size of 68 µm in the former cooling method supports the finding relative to 99 µm in the naturally cooled specimen (Figure 26). On the other hand, the cold water-cooled sample had the highest average grain size in such a zone with values between 14.2 µm and 15.2 µm. This is further explained by the limited stirring induced thermal input to the seamless tube resulting in static recrystalized zone [66].

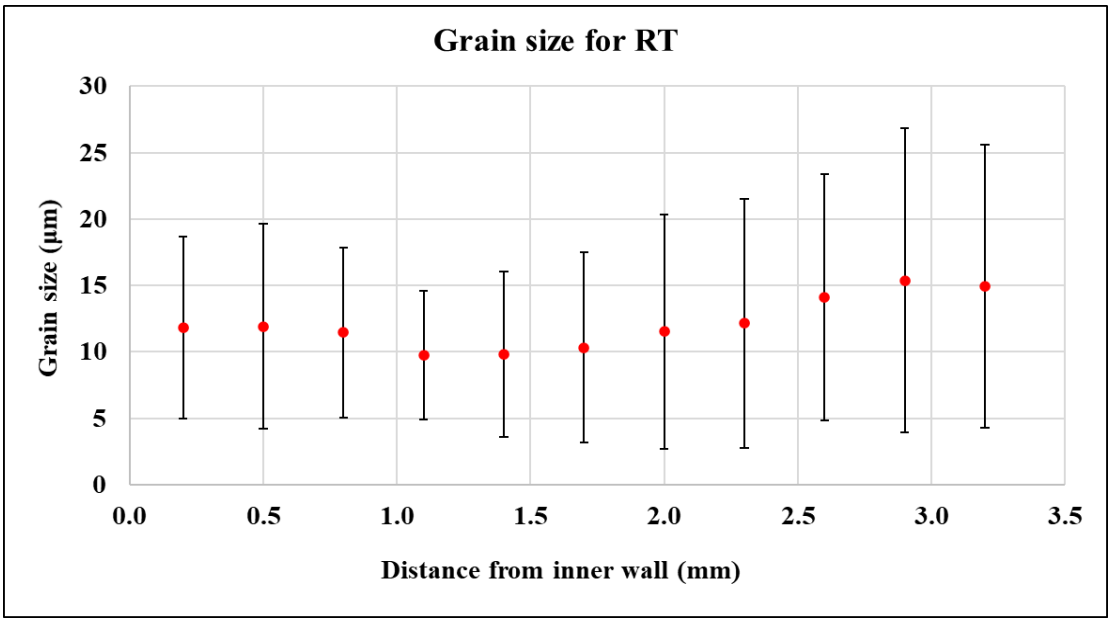

Figure 24: Grain size distribution in room temperature cooled medium

Although the thermo-mechanical effect is not adequate in the far proximity distant zone of the material which does not activate the full growth of grains with low dislocation densities, refinement in the cooled tube by air is present through a peak grain value of 50 µm (Figure 26). This is due to the apparent effect of recrystallization at the outer surface since the traces of high heat and strain inputs are still present after the recrystallization period is over relative to the room temperature and cold water-cooled (Figure 25) tubes where inadequate formation of new grains are present resulting in the highest peak grain sizes of 87 µm and 90 µm (Figure 26), respectively.

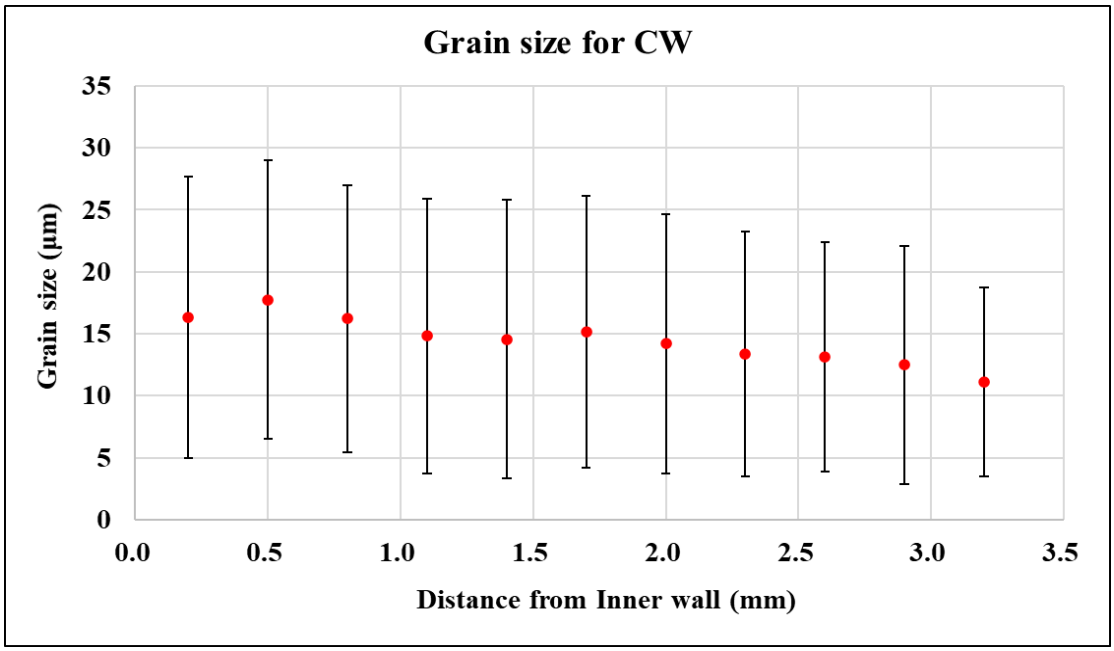

Figure 25: Grain size distribution in cold water cooled medium

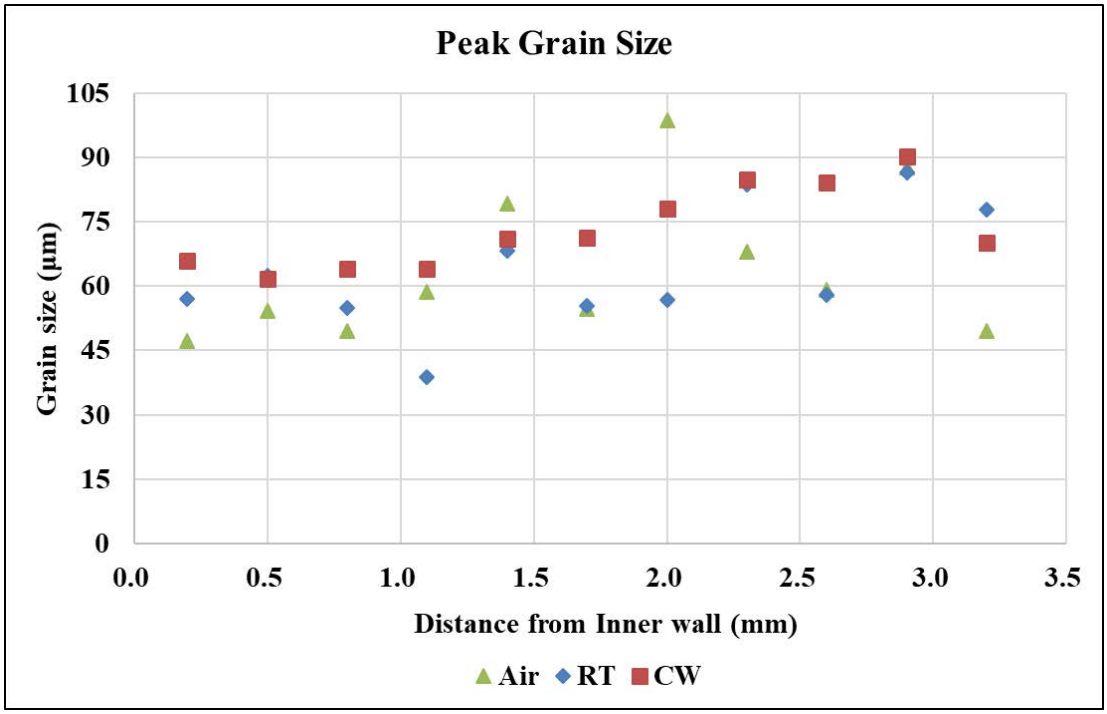

Figure 26: Peak grain size distribution across all mediums

Figures 27a,b present the as received material and it can distinguished from the other remaining images of Figure 27 in terms of their high heterogeneity. Stirring zone related micrographs show homogeneity across the inner zone (Figure 27c) of equiaxed grains while it can be seen that some grain inhomogeneities in the intermediate zone

take place (Figure 27d) with slightly higher grains besides partial grains from the dynamically recrystalized zone. This indicates a decline in the exposure of intense plastic deformation accompanied with elevated temperatures. The outward zone (Figure 27e) perfectly describes a heterogeneous grain structure similar to the as received material with fine grains among differently sized coarse grains reaching up to 90 µm throughout the differently cooled AZ31-B specimens.

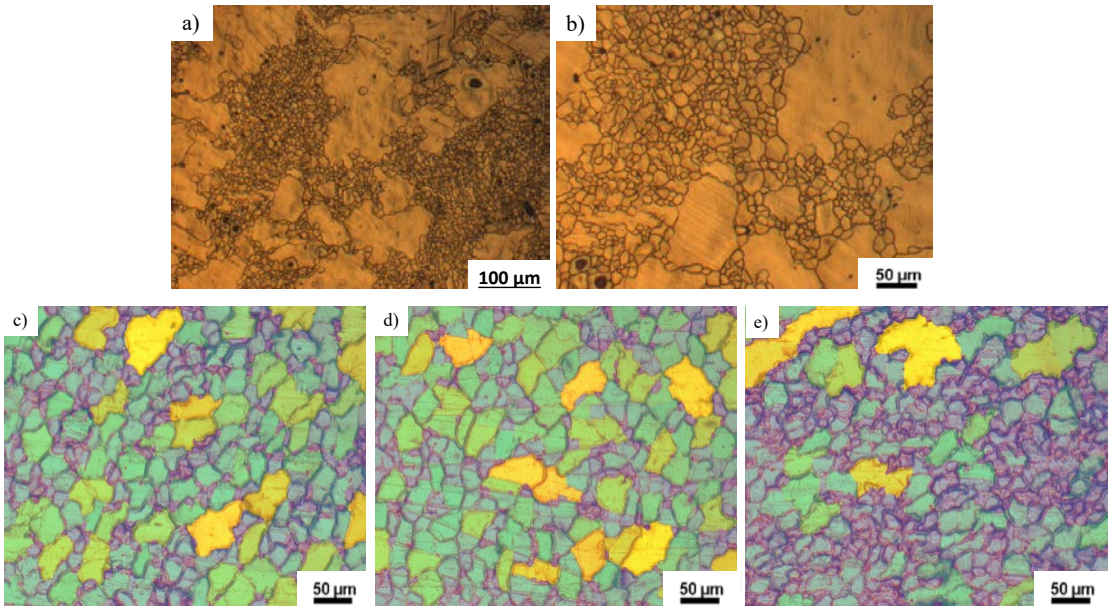

Figure 27: a,b) grain structure of the as received material and c) in the stirring zone and d) middle zone and e) in the outer zone of the CW processed tube

Furthermore, it can be noticed that the cooling rate, change in temperature with time after the peak thermal value, varies among the three samples, in which air has a cooling rate of 0.085 °C/sec while CW and RT have values of 1.40 °C/sec and 1.72 °C/sec, respectively. Relating the above with the thermal history and microstructural characterization, favorable effects were achieved with higher (rapid) cooling rates with respect to the grain size and this is the case with RT as it has the highest heat capacity implying large absorption of the high self-generated heat. However, its impact was inconsiderable in terms of the mechanical properties, UTS and ductility.

Finally, one of the productivity indicators, power consumption, showed no major difference at all although the effect of the cooling rate is present as values of 200.0 kW and 201.6 kW for the air and RT cooling mediums are recorded while the CW had a power value of 202.9 kW. While it is expected a see a variation among the

above values in Figure 28 since the stirring tool needs more power to extrude the tube at cooler environments as it relates to the temperature [59].

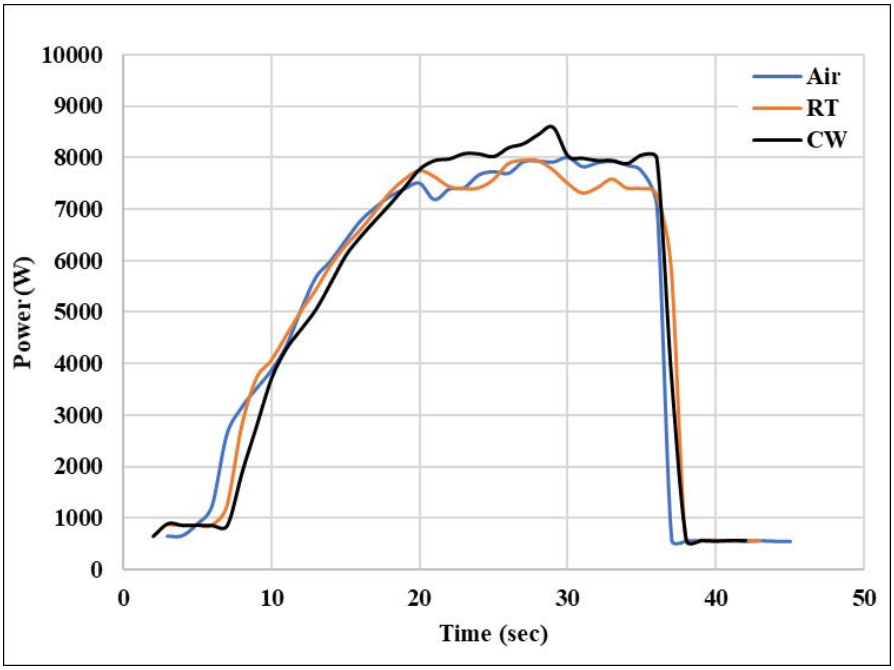

Figure 28: Power consumption distribution for each cooling method

Chapter 6. Conclusion and Future Work

In this research, Response Surface Methodology statistical method is used for the Friction Stir Back Extrusion of AZ31-B Magnesium alloy to predict and optimize the mechanical properties namely, ultimate tensile strength, percent elongation and toughness on top of power consumption and cycle time as productivity indicators. In addition, submerged FSBE process with the mechanical properties, thermal history, power consumption profiles and microstructure were characterized. Accordingly, the following are induced:

- The developed mathematical models had a coefficient of determination of 71%, 63%, 61% and 99% for ultimate tensile strength, toughness, power consumption and cycle time, respectively. The variation of FSBE process parameters had a parabolic influence on the responses and the models were validated through ANOVA.
- Using desirability multi-response optimization, the optimal maximized mechanical properties are identified to be 1767 rpm and 102 mm/min, while the latter properties with minimizing the production indicators give the optimal process conditions of 2000 rpm and 116 mm/min. A maximum of 10% prediction error was achieved for the optimal mechanical conditions.
- The recorded temperature profiles in the middle of the extrusion die during FSBE showed a peak temperature of 230 °C in the die for the conditions of 2000 rpm and 60 mm/min. This is an indication of high heat input that deteriorates the mechanical properties due to grain growth.
- Temperature profiles of the submerged FSBE tests of air, room temperature and cold water showed peak values of 208°C, 155 °C and 81 °C, respectively at 2000 rpm and 90 mm/min.
- The differences in the ultimate tensile strength and percent elongation are not significant since the P-values of the 2 sample T-tests revealed statistical insignificance in the liquid water cooling medium besides natural cooling. Likewise, the consumed power variations were very minimal between the above mediums.
- Room temperature cooled specimen proves to have enough generated temperature in the deformed zone as it induced sufficient extrusion thermal

input which means minimal grain growth prominent by the finest average grain size of 9.8 μm in the intermediate zone.

- Cold water sample implies the highest average grain size across all cooling methods in the middle zone due to the low supply of high heat and strain to the material. This in turns did not push the limits in the recrystallization process resulting in average grain size of 14.7 μm.
- The room temperature test proved itself with the highest cooling rate, 1.72 °C/sec, that is inversely proportional with the resulting grain size refinement directing attention towards the occurred suitable recovery and recrystallization with minimal grain growth.

Since the percent elongation did not change significantly by the change in feed rate or rotational speed in the optimization of FSBE, expanding the window of experimentations by increasing feed rate and spindle speed might induce a statistically significant change. Moreover, varying the process parameters in the cold-water condition of the underwater FSBE process by either increasing the rotational speed or reducing the feed rate could have a desirable effect on the grain size and distribution. Exploration of the tension-compression yield asymmetry and obtaining the Lankford coefficient for the extruded tubes which characterizes the material's asymmetry and anisotropy can be a part of the future investigation. In addition, the study of the formability condition of the seamless tubes through 3-point bending experiments besides fractography characterization of the fractured tensile and 3-point bending specimens.

References

[1] W. M. Thomas, E. D. Nicholas, S. B. Jones. “Forming metallic composite materials by urging base materials together under shear.” U.S. Patent 5262123A, Jun. 6, 1990.

[2] Monroe. "Comparing the Different Types of Extrusion Processes.", Internet: https://monroeengineering.com/blog/comparing-the-different-types-of-extrusion-processes/, Jan. 18, 2019 [Oct. 23, 2020]

[3] S. Whalen, V. Joshi, N. Overman, D. Caldwell, C. Lavender, and T. Skszek, "Scaled-Up Fabrication of Thin-Walled ZK60 Tubing Using Shear Assisted Processing and Extrusion (ShAPE)," in *Magnesium Technology 2017*: Springer International Publishing: Cham, 2017, pp. 315-321.

[4] M. Cabibbo, A. Forcellese, E. Santecchia, C. Paoletti, S. Spigarelli, and M. Simoncini, "New Approaches to Friction Stir Welding of Aluminum Light-Alloys," *Metals,* vol. 10, pp. 233, 2020.

[5] M. A. Wahid, Z. A. Khan, and A. N. Siddiquee, "Review on underwater friction stir welding: A variant of friction stir welding with great potential of improving joint properties," *Transactions of Nonferrous Metals Society of China,* vol. 28, pp. 193-219, 2018.

[6] M. Sucharitha, B. R. Sankar, and P. Umamaheswarrao, "A Review on Submerged Friction Stir Welding of Light Weight Alloys," vol. 954, pp. 012014 2020.

[7] S. L. Semiatin, *vol. 14A: Metalworking: bulk forming*, ASM Handbook, ASM International, Materials Park, Ohio, US, 2006.

[8] F. Abu-Farha, "A preliminary study on the feasibility of friction stir back extrusion," *Scripta Materialia,* vol. 66, pp. 615-618, 2012.

[9] F. Abu-Farha. "Extruded Tubing via Friction Stir Forming." U.S. Patent Appl. 61/547148, Oct. 14, 2011.

[10] J. L. Milner and F. Abu-Farha, "Friction Stir Back Extrusion of Mg AZ31B-F: A Preliminary Investigation," in *Magnesium Technology 2014*: John Wiley & Sons, Inc.: Hoboken, NJ, USA, 2014, pp. 497-503, 2014.

[11] S. Rajakumar, C. Muralidharan, and V. Balasubramanian, "Influence of friction stir welding process and tool parameters on strength properties of AA7075-T6 aluminium alloy joints," *Materials and Design,* vol. 32, pp. 535-549, 2011.

[12] M. Ghosh, K. Kumar, S. V. Kailas, and A. K. Ray, "Optimization of friction stir welding parameters for dissimilar aluminum alloys," *Materials and Design,* vol. 31, pp. 3033-3037, 2010.

[13] D. C. Montgomery, *Design and analysis of experiments*. New York: Wiley, 1997.

[14] E. C. Harrington. “The Desirability Function.” in Industrial Quality Control, 10th ed., vol.21, 1965, pp.494-498.

[15] H. Pham, *Springer handbook of engineering statistics*, Springer Handbooks, Springer-Verlag, London, UK, 2006.

[16] M. Alkhader, M. Nazzal, and K. Louca, "Design of bending dominated lattice architectures with improved stiffness using hierarchy," *Proceedings of the Institution of Mechanical Engineers, Part C: Journal of Mechanical Engineering Science,* vol. 233, pp. 3976-3993, 2018.

[17] A. Ghandehariun, M. Nazzal, H. A. Kishawy, and U. Umer, "On modeling the deformations and tool-workpiece interactions during machining metal matrix composites," *The International Journal of Advanced Manufacturing Technology,* vol. 91, pp. 1507-1516, 2017.

[18] M. Valente, D. Marini, V. Genova, A. Quitadamo, F. Marra, and G. Pulci, "Lightweight metallic matrix composites: Development of new composites material reinforced with carbon structures," *Journal of Applied Biomaterials & Functional Materials,* vol. 17, pp. 2280800019840294, 2019.

[19] W. Monteiro, S. J. Buso, and L. V. da Silva, "Application of Magnesium Alloys in Transport," *New Features on Magnesium Alloys*, Nov. 2012.

[20] Metalpedia. "Magnesium: applications and uses." Internet: http://metalpedia.asianmetal.com/metal/magnesium/application.shtml, [Nov. 10, 2020].

[21] F. K. Abu-Farha, L. G. Hector, and M. A. Nazzal, "On the Development of Viable Cruciform-Shaped Specimens: Towards Accurate Elevated Temperature Biaxial Testing of Lightweight Materials," *Key Engineering Materials,* vol. 433, pp. 93-101, 2010.

[22] F. S. Jarrar and M. A. Nazzal, "Inclination Angle Effect on the Thickness Distribution in a Superplastic Formed Long Rectangular Pan," *Materials Science Forum,* vol. 735, pp. 155-161, 2013.

[23] M. K. Khraisheh, F. K. Abu-Farha, M. A. Nazzal, and K. J. Weinmann, "Combined Mechanics-Materials Based Optimization of Superplastic Forming of Magnesium AZ31 Alloy," *CIRP Annals,* vol. 55, pp. 233-236, 2006.

[24] M. Nazzal, F. Abu-Farha, and R. Curtis, "Finite Element Simulations for Investigating the Effects of Specimen Geometry in Superplastic Tensile Tests," *Journal of Materials Engineering and Performance,* vol. 20, pp. 865-876, 2011.

[25] M. A. Nazzal, "Stability analysis and finite element simulations of superplastic forming in the presence of hydrostatic pressure," *AIP Conference Proceedings,* vol. 1957, p. 050006, 2018.

[26] M. A. Nazzal and F. K. Abu-Farha, "Finite Element Modeling of Superplastic Forming of Tubular Shapes," *Key Engineering Materials,* vol. 433, pp. 179-184, 2010.

[27] M. A. Nazzal and A. G. Al Sabouni, "The effects of pressure control technique on hot gas blow forming of Mg AZ31 sheets," *International Journal of Material Forming,* vol. 12, pp. 519-533, 2019.

[28] M. A. Nazzal and M. K. Khraisheh, "The Effects of Stress State and Cavitation on Deformation Stability During Superplastic Forming," *Journal of Materials Engineering and Performance,* vol. 16, pp. 200-207, 2007.

[29] M. A. Nazzal, M. K. Khraisheh, and F. K. Abu-Farha, "The effect of strain rate sensitivity evolution on deformation stability during superplastic forming," *Journal of Materials Processing Technology,* vol. 191, pp. 189-192, 2007.

[30] M. A. Nazzal, M. K. Khraisheh, and B. M. Darras, "Finite element modeling and optimization of superplastic forming using variable strain rate approach," *Journal of Materials Engineering and Performance,* vol. 13, pp. 691-699, 2004.

[31] J. L. Milner and F. Abu-Farha, "On the manufacture of lightweight alloy tubes via friction stir back extrusion: process evaluation and material performance," in ASME 2014 International Manufacturing Science and Engineering Conference collocated with the JSME 2014 International Conference on Materials and Processing and the 42nd North American Manufacturing

Research Conference, 2014, Volume 2: Processing, V002T02A085.
[32] H. Cai, "*Fiabilisation de convertisseurs analogique-numérique à modulation Sigma-Delta*," Ph.D. dissertation, Dept. Elect. Eng., Institute Polytechnique de Paris, Pairs, 2013.
[33] M. Maalekian, "Friction welding – critical assessment of literature," *Science and Technology of Welding and Joining,* vol. 12, pp. 738-759, 2007.
[34] C. Bampton, "Effects of friction stir welding on microstructure of 7075 aluminum," *Scripta Materialia,* vol. 36, pp. 69-75, 1997.
[35] M. W. Mahoney, C. G. Rhodes, J. G. Flintoff, W. H. Bingel, and R. A. Spurling, "Properties of friction-stir-welded 7075 T651 aluminum," *Metallurgical and Materials Transactions A,* vol. 29, pp. 1955-1964, 1998.
[36] P. Cavaliere, G. Campanile, F. Panella, and A. Squillace, "Effect of welding parameters on mechanical and microstructural properties of AA6056 joints produced by Friction Stir Welding," *Journal of Materials Processing Tech.,* vol. 180, pp. 263-270, 2006.
[37] O. Hatamleh, J. Lyons, and R. Forman, "Laser and shot peening effects on fatigue crack growth in friction stir welded 7075-T7351 aluminum alloy joints," *International Journal of Fatigue,* vol. 29, pp. 421-434, 2007.
[38] O. Mypati et al., "Enhancement of joint strength in friction stir lap welding between AA6061 and AISI 304 by adding diffusive coating agents," *Proceedings of the Institution of Mechanical Engineers, Part B: Journal of Engineering Manufacture,* vol. 234, pp. 204-217, 2020.
[39] M. A. Wahid, Z. A. Khan, A. N. Siddiquee, R. Shandley, and N. Sharma, "Analysis of process parameters effects on underwater friction stir welding of aluminum alloy 6082-T6," *Proceedings of the Institution of Mechanical Engineers,* vol. 233, pp. 1700-1710, 2018/
[40] R. S. Mishra, M. W. Mahoney, S. X. McFadden, N. A. Mara, and A. K. Mukherjee, "High strain rate superplasticity in a friction stir processed 7075 Al alloy," *Scripta Materialia,* vol. 42, pp. 163-168, 1999.
[41] M. S. Weglowski, S. Dymek, and C. B. Hamilton, "Experimental investigation and modelling of Friction Stir Processing of cast aluminium alloy AlSi9Mg," *Bulletin of the Polish Academy of Sciences: Technical Sciences,* vol. 61, pp. 893-904, 2013.
[42] Y. Zhao, H. Guo, M. W. Fu, Y. Ning, and Z. Yao, "Fabrication of bulk ultrafine grained titanium alloy via equal channel angular pressing based thermomechanical treatment," *Materials and Design,* vol. 46, pp. 889-894, 2013.
[43] M. Arzaghi et al., "Microstructure, texture and mechanical properties of aluminum processed by high-pressure tube twisting," *Acta Materialia,* vol. 60, pp. 4393-4408, 2012.
[44] S. Verma and J. P. Misra, "Effect of process parameters on temperature and force distribution during friction stir welding of armor-marine grade aluminum alloy," *Proceedings of the Institution of Mechanical Engineers, Part B: Journal of Engineering Manufacture,* p. 095440542094910, 2020.
[45] M. P. Iqbal, R. K. Vishwakarma, S. K. Pal, and P. Mandal, "Influence of plunge depth during friction stir welding of aluminum pipes," *Proceedings of the Institution of Mechanical Engineers, Part B: Journal of Engineering Manufacture,* p. 095440542094975, 2020.
[46] R. Jain, S. K. Pal, and S. B. Singh, "Investigation on effect of pin shapes on

temperature, material flow and forces during friction stir welding: A simulation study," *Proceedings of the Institution of Mechanical Engineers,* vol. 233, no. 9, pp. 1980-1992, 2019.

[47] G. Rambabu, D. B. Naik, C. H. V. Rao, K. S. Rao, and G. M. Reddy, "Optimization of friction stir welding parameters for improved corrosion resistance of AA2219 aluminum alloy joints," *Defence Technology,* vol. 11, pp. 330-337, 2015.

[48] C. Zhang, G. Huang, Y. Cao, X. Wu, X. Huang, and Q. Liu, "Optimization of Tensile and Corrosion Properties of Dissimilar Friction Stir Welded AA2024-7075 Joints," *Journal of Materials Engineering and Performance,* vol. 28, pp. 183-199, 2019.

[49] R. H. Kabiri and M. S. Ehsan, "Optimization of FSW lap joining of pure copper using Taguchi method and grey relational analysis," vol. 6, pp. 056525, 2019.

[50] A. Kumar, M. K. Khurana, and G. Singh, "Modeling and Optimization of Friction Stir Welding Process Parameters for Dissimilar Aluminium Alloys," *Materials Today: Proceedings: Part 3,* vol. 5, pp. 25440-25449, 2018.

[51] Y. S. Abbasi, S. I. Butt, G. Hussain, S. H. Imran, A. M. Khan, and R. A. Baseer, "Optimization of parameters for micro friction stir welding of aluminum 5052 using Taguchi technique," *The International Journal of Advanced Manufacturing Technology,* vol. 102, pp. 369-378, 2019.

[52] C. C. de Castro, A. H. Plaine, N. G. de Alcântara, and J. F. dos Santos, "Taguchi approach for the optimization of refill friction stir spot welding parameters for AA2198-T8 aluminum alloy," *The International Journal of Advanced Manufacturing Technology,* vol. 99, pp. 1927-1936, 2018.

[53] A. N. Colmenero et al., "Optimization of friction stir spot welding process parameters for Al-Cu dissimilar joints using the energy of the vibration signals," *The International Journal of Advanced Manufacturing Technology,* vol. 100, pp. 2795-2802, 2019.

[54] K. K. Babu et al., "Parameter optimization of friction stir welding of cryorolled AA2219 alloy using artificial neural network modeling with genetic algorithm," *The International Journal of Advanced Manufacturing Technology,* vol. 94, pp. 3117-3129, 2018.

[55] P. Praveen and P. K. Yarlagadda, "Meeting challenges in welding of aluminum alloys through pulse gas metal arc welding," *Journal of Materials Processing Tech.,* vol. 164, pp. 1106-1112, 2005.

[56] W. A. Baeslack, K. V. Jata, and T. J. Lienert, "Structure, properties and fracture of friction stir welds in a high-temperature Al-8.5Fe-1.3V-1.7Si alloy (AA-8009)," *Journal of Materials Science,* vol. 41, pp. 2939-2951, 2006.

[57] M. Cabibbo, H. J. McQueen, E. Evangelista, S. Spigarelli, M. Di Paola, and A. Falchero, "Microstructure and mechanical property studies of AA6056 friction stir welded plate," *Materials Science & Engineering A,* vol. 460, pp. 86-94, 2007.

[58] F. Rui-dong, S. Zeng-qiang, S. Rui-cheng, L. Ying, L. Hui-jie, and L. Lei, "Improvement of weld temperature distribution and mechanical properties of 7050 aluminum alloy butt joints by submerged friction stir welding," *Materials and Design,* vol. 32, pp. 4825-4831, 2011.

[59] B. Darras and E. Kishta, "Submerged friction stir processing of AZ31 Magnesium alloy," *Materials and Design,* vol. 47, pp. 133-137, 2013.

[60] M. A. Mofid, A. Abdollah-zadeh, F. M. Ghaini, and C. H. Gür, "Submerged

Friction-Stir Welding (SFSW) Underwater and Under Liquid Nitrogen: An Improved Method to Join Al Alloys to Mg Alloys," *Metallurgical and Materials Transactions,* vol. 43, pp. 5106-5114, 2012.

[61] H. Zhang and H. Liu, "Characteristics and Formation Mechanisms of Welding Defects in Underwater Friction Stir Welded Aluminum Alloy," *Metallography, Microstructure, and Analysis: Application and Innovation for Metals, Alloys, and Engineered Materials,* vol. 1, pp. 269-281, 2012.

[62] R. Chandran and S. K. V. Santhanam, "Submerged Friction Stir Welding of 6061-T6 Aluminium Alloy under Different Water Heads," *Materials Research,* vol. 21, pp. 012014 ,2018.

[63] R. Chandran and S. K. V. Santhanam, "Modelling and optimization of submerged friction stir welding parameters for AA6061-T6 alloy using RSM," *Kovove Materialy,* vol. 54, pp. 297-304, 2016.

[64] G. Peng, Q. Yan, J. Hu, P. Chen, Z. Chen, and T. Zhang, "Effect of Forced Air Cooling on the Microstructures, Tensile Strength, and Hardness Distribution of Dissimilar Friction Stir Welded AA5A06-AA6061 Joints," *Metals,* vol. 9, pp. 304, 2019.

[65] A. Menard et al., "Friction stir back extrusion: Preliminary investigations on through-wall characteristics for AL-1100-O," *ASME International Mechanical Engineering Congress and Exposition, Proceedings (IMECE),* vol. 2, 2018.

[66] M. S. Khorrami and M. Movahedi, "Microstructure evolutions and mechanical properties of tubular aluminum produced by friction stir back extrusion," *Materials and Design,* vol. 65, pp. 74-79, 2015.

[67] M. H. Saad, M. A. Nazzal, and B. M. Darras, "A general framework for sustainability assessment of manufacturing processes," *Ecological Indicators,* vol. 97, pp. 211-224, 2019.

[68] M. H. Saad, B. M. Darras, and M. A. Nazzal, "Evaluation of Welding Processes Based on Multi-dimensional Sustainability Assessment Model," *International Journal of Precision Engineering and Manufacturing - Green Technology,* pp. 1-19, 2020.

[69] M. H. Saad, O. M. Jarrah, M. A. Nazzal, B. M. Darras, and H. A. Kishawy, "Sustainability-based evaluation of Friction Stir Back Extrusion of seamless tubular shapes," *Journal of Cleaner Production,* vol. 267, pp. 121972, 2020.

[70] N. Mathew, I. Dinaharan, S. J. Vijay, and N. Murugan, "Microstructure and Mechanical Characterization of Aluminum Seamless Tubes Produced by Friction Stir Back Extrusion," *Transactions of the Indian Institute of Metals,* vol. 69, pp. 1811-1818, 2016.

[71] A. Pandarkar, M. D. Goel, and M. S. Hora, "Axial crushing of hollow and foam filled tubes: An overview," *Sādhanā: Published by the Indian Academy of Sciences,* vol. 41, pp. 909-921, 2016.

[72] O. M. Jarrah. “Investigation of Friction Stir Back Extrusion.” M.Sc. thesis, American University of Sharjah, UAE, 2019.

[73] W. J. Emblom et al., "Friction Stir Back Extrusion: Tooling and Process Design for AL-1100-O," in *Volume 4: Processes*: American Society of Mechanical Engineers, 2018.

[74] G. Jamali, S. Nourouzi, and R. Jamaati, "Microstructure and mechanical properties of AA6063 aluminum alloy wire fabricated by friction stir back extrusion (FSBE) process," *International Journal of Minerals, Metallurgy, and Materials,* vol. 26 pp. 1005-1012, 2019.

[75] J. L. Milner and F. Abu-Farha, "Microstructural Evolution and Its Relationship to the Mechanical Properties of Mg AZ31B Friction Stir Back Extruded Tubes," in *Magnesium Technology 2014*: John Wiley & Sons, Inc.: Hoboken, NJ, USA, 2014, pp. 263-268, 2014.

[76] G. Derringer and R. Suich, "Simultaneous Optimization of Several Response Variables," *Journal of Quality Technology,* vol. 12, pp. 214-219, 1980.

[77] Aircraft Materials. *"Magnesium Alloy AZ31B."* Internet: https://www.aircraftmaterials.com/data/magnesium/az31b.html. [Nov. 5, 2019].

[78] M. Wang, B. Y. Zong, and G. Wang, "Grain growth in AZ31 Mg alloy during recrystallization at different temperatures by phase field simulation," *Computational Materials Science,* vol. 45, pp. 217-222, 2009.

[79] R. S. Mishra and Z. Y. Ma, "Friction stir welding and processing," *Materials Science and Engineering,* vol. 50, pp. 1-78, 2005.

[80] K. Huang and R. E. Logé, "A review of dynamic recrystallization phenomena in metallic materials," *Materials & Design,* vol. 111, pp. 548-574, 2016.

[81] D. Raabe, "23 - Recovery and Recrystallization: Phenomena, Physics, Models, Simulation," in *Physical Metallurgy (Fifth Edition)*. Oxford: Elsevier, 2014, pp. 2291

[82] Y. Harai, M. Kai, K. Kaneko, Z. Horita, and T. G. Langdon, "Microstructural and Mechanical Characteristics of AZ61 Magnesium Alloy Processed by High-Pressure Torsion," *MATERIALS TRANSACTIONS,* vol. 49, pp. 76-83, 2008.

[83] H. K. Lin, J. C. Huang, and T. G. Langdon, "Relationship between texture and low temperature superplasticity in an extruded AZ31 Mg alloy processed by ECAP," *Materials Science and Engineering: A,* vol. 402, pp. 250-257, 2005.

Appendix A: MATLAB Code

```
clc;
clear all;
close all;

% Design factors: x = [N ; f]
% Canonical variables: w = [w1 ; w2]

% UTS Eigenvalues
UTSb = [7.41; 0];
UTSB = [-9.36 0; 0 -16.16];
UTSxs= -0.5*((UTSB)^-1)*UTSb;
UTSys = 262.8 + 0.5*transpose(UTSxs)*UTSb;
UTSEigenvalues = eig(UTSB);

fprintf('UTS_y = %2.3f %2.2f*w1^2 %2.2f*w2^2\n',UTSys,UTSEigenvalues)

% Toughness Eigenvalues
Toughnessb = [0.012; 0.394];
ToughnessB = [0 -0.00008/2; -0.00008/2 -0.0112];
Toughnessxs= -0.5*((ToughnessB)^-1)*Toughnessb;
Toughnessys = -6.9 + 0.5*transpose(Toughnessxs)*Toughnessb;
ToughnessEigenvalues = eig(ToughnessB);

fprintf('Toughness_y = %2.2f %2.4f*w1^2 +
%2.10f*w2^2\n',Toughnessys,ToughnessEigenvalues)

% Power Consumption Eigenvalues
Powerb = [0; -36.92];
PowerB = [-28.1 0; 0 30.8];
Powerxs= -0.5*((PowerB)^-1)*Powerb;
```

```
Powerys = 138.37 + 0.5*transpose(Powerxs)*Powerb;
PowerEigenvalues = eig(PowerB);

fprintf('Power_y = %2.2f %2.2f*w1^2 + %2.2f*w2^2\n',Powerys,PowerEigenvalues)
```

```
UTS_y = 264.267 -16.16*w1^2 -9.36*w2^2
Toughness_y = -199.80 -0.0112*w1^2 - 0.0000001429*w2^2
Power_y = 127.31 -28.10*w1^2 + 30.80*w2^2
```

Published with MATLAB® R2019b

Appendix B: Residual Plots

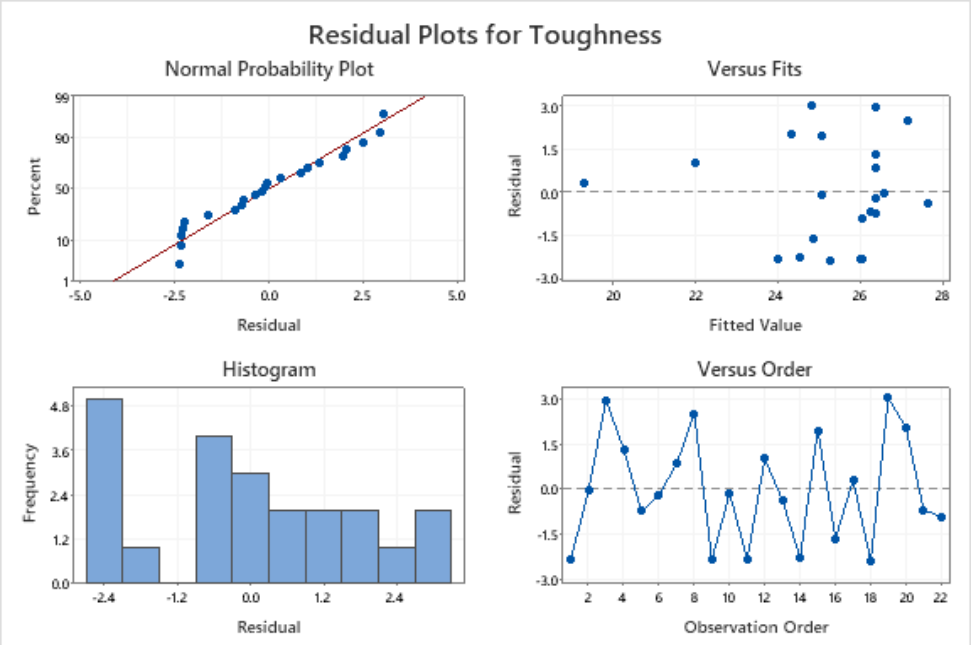

Figure 29: Residual plots for toughness

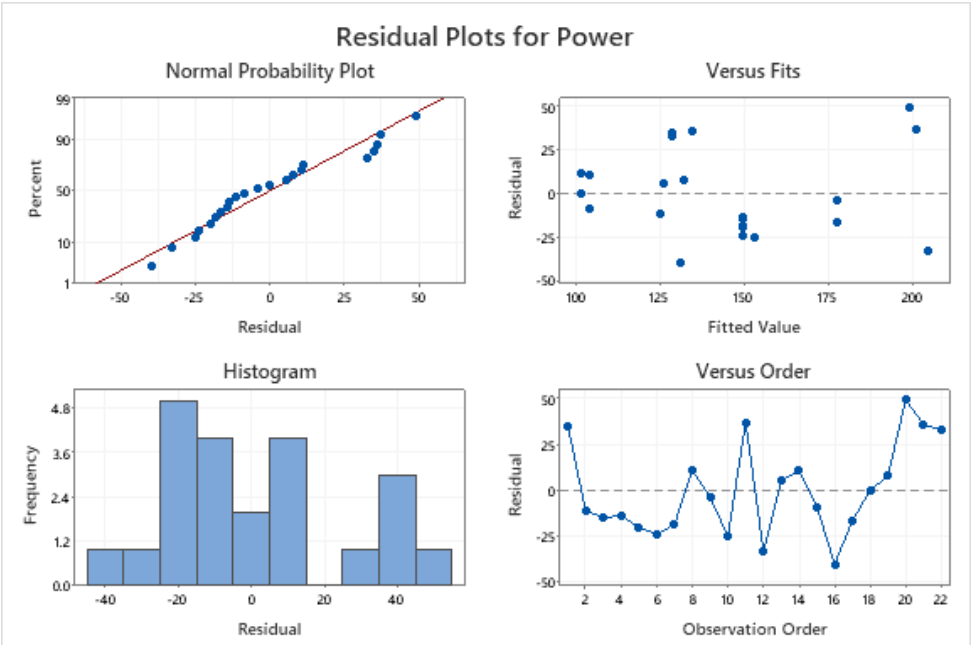

Figure 30: Residual plots for power consumption

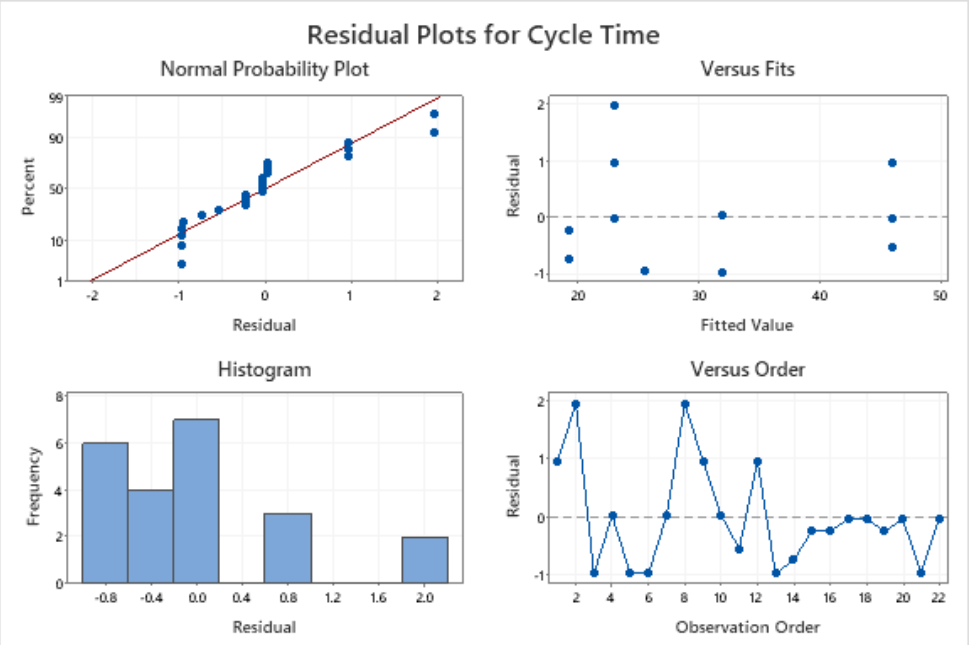

Figure 31: Residual plots for cycle time

Appendix C: 2 Sample T-tests

a)

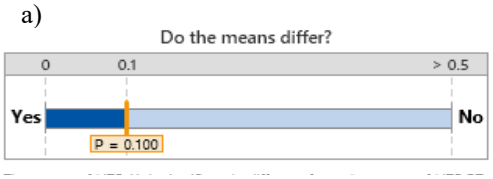

Individual Samples

Statistics	UTS Air	UTS RT
Sample size	2	2
Mean	263.6	257.89
90% CI	(260.6, 266.6)	(253.06, 262.73)
Standard deviation	0.67882	1.0819

b)

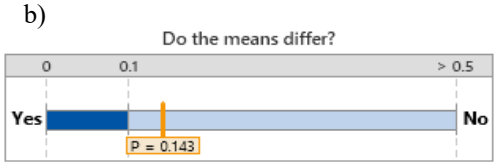

Individual Samples

Statistics	UTS Air	UTS CW
Sample size	2	2
Mean	263.6	261.49
90% CI	(260.6, 266.6)	(261.36, 261.62)
Standard deviation	0.67882	0.028284

c)

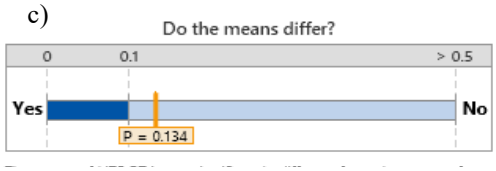

Individual Samples

Statistics	UTS RT	UTS CW
Sample size	2	2
Mean	257.89	261.49
90% CI	(253.1, 262.7)	(261.36, 261.62)
Standard deviation	1.0819	0.028284

Figure 32: 2 Sample T-tests for UTS in a) Air with RT and b) Air with CW and c) RT with CW

a)

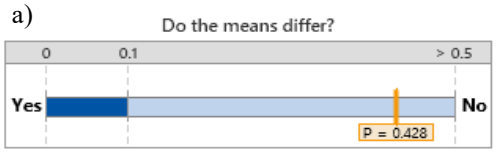

Individual Samples

Statistics	%EL Air	%EL RT
Sample size	2	2
Mean	12.823	10.22
90% CI	(0.0503, 25.60)	(7.3157, 13.124)
Standard deviation	2.8610	0.65054

b)

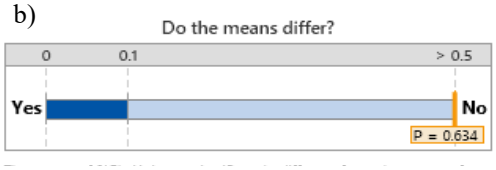

Individual Samples

Statistics	%EL Air	%EL CW
Sample size	2	2
Mean	12.823	11.505
90% CI	(0.0503, 25.60)	(10.021, 12.989)
Standard deviation	2.8610	0.33234

c)

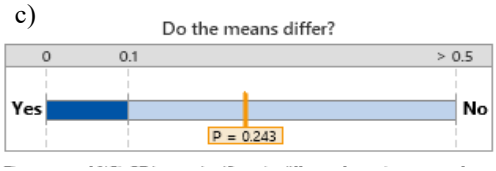

Individual Samples

Statistics	%EL RT	%EL CW
Sample size	2	2
Mean	10.22	11.505
90% CI	(7.316, 13.12)	(10.021, 12.989)
Standard deviation	0.65054	0.33234

Figure 33: 2 Sample T-tests for %EL in a) Air with RT and b) Air with CW and c) RT with CW

Vita

Abdulla Taoufik Alhourani was born in 1996, in Dubai, United Arab Emirates. He had his primary and secondary education in Sharjah, UAE. He completed his internship at Air Arabia in Sharjah and received his B.Sc. degree in Mechanical Engineering from the American University of Sharjah (AUS) in May 2018.

In September 2018, he joined the Mechanical Engineering master's program in AUS where he served as a graduate teaching assistant from 2018 to 2020. His research interests are in the track of design and manufacturing and specifically in the manufacturing of metal alloys such as Magnesium alloys through FSBE.

Mr. Alhourani is a member of the American Society of Mechanical Engineers (ASME).